

Contents lists available at ScienceDirect

Biomaterials

journal homepage: www.elsevier.com/locate/biomaterials





Skin repair and infection control in diabetic, obese mice using bioactive laser-activated sealants

Shubham Pallod ^{a,b}, Rodrigo Aguilera Olvera ^c, Deepanjan Ghosh ^b, Lama Rai ^{a,d}, Souzan Brimo ^{a,e}, Weston DeCambra ^f, Harsh Girish Sant ^{a,g}, Eron Ristich ^{f,h}, Vanshika Singh ^{a,e}, Muhammad Raisul Abedin ^a, Nicolas Chang ^{a,e}, Jeffery L. Yarger ^f, Jung Keun Lee ⁱ, Jacquelyn Kilbourne ^j, Jordan R. Yaron ^a, Shelley E. Haydel ^{c,k}, Kaushal Rege ^{a,b,g,*}

- ^a Center for Biomaterials Innovation and Translation, Biodesign Institute, Arizona State University, USA
- b Biological Design Graduate Program, School for Engineering of Matter, Transport, and Energy, Arizona State University, USA
- ^c Center for Bioelectronics and Biosensors, Biodesign Institute, Arizona State University, USA
- ^d College of Health Solutions, Arizona State University, USA
- ^e Biomedical Engineering, School for Biological and Health Systems Engineering, Arizona State University, USA
- f School of Molecular Sciences, Arizona State University, USA
- g Chemical Engineering, School for Engineering of Matter, Transport, and Energy, Arizona State University, USA
- ^h School of Computing and Augmented Intelligence, Arizona State University, USA
- i Departments of Pathology and Population Medicine, Midwestern University, College of Veterinary Medicine, 5725 West Utopia Rd., Glendale, AZ, 85308, USA
- Department of Animal Care Technologies, Arizona State University, USA
- k School of Life Sciences, Arizona State University, 501 E. Tyler Mall ECG 303, Tempe, AZ, 85287-6106, USA

ARTICLE INFO

Keywords: Biomaterials Skin sealing Infection control Wound healing

ABSTRACT

Conventional wound approximation devices, including sutures, staples, and glues, are widely used but risk of wound dehiscence, local infection, and scarring can be exacerbated in these approaches, including in diabetic and obese individuals. This study reports the efficacy and quality of tissue repair upon photothermal sealing of full-thickness incisional skin wounds using silk fibroin-based laser-activated sealants (LASEs) containing copper chloride salt (Cu-LASE) or silver nanoprisms (AgNPr-LASE), which absorb and convert near-infrared (NIR) laser energy to heat. LASE application results in rapid and effective skin sealing in healthy, immunodeficient, as well as diabetic and obese mice. Although lower recovery of epidermal structure and function was seen with AgNPr-LASE sealing, likely because of the hyperthermia induced by laser and presence of this material in the wound space, this approach resulted in higher enhancement in recovery of skin biomechanical strength compared to sutures and Cu-LASEs in diabetic, obese mice. Histological and immunohistochemical analyses revealed that AgNPr-LASEs resulted in significantly lower neutrophil migration to the wound compared to Cu-LASEs and sutures, indicating a more muted inflammatory response. Cu-LASEs resulted in local tissue toxicity likely because of effects of copper ions as manifested in the form of a significant epidermal gap and a 'depletion zone', which was a region devoid of viable cells proximal to the wound. Compared to sutures, LASE-mediated sealing, in later stages of healing, resulted in increased angiogenesis and diminished myofibroblast activation, which can be indicative of lower scarring, AgNPr-LASE loaded with vancomycin, an antibiotic drug, significantly lowered methicillin-resistant Staphylococcus aureus (MRSA) load in a pathogen challenge model in diabetic and obese mice and also reduced post-infection inflammation of tissue compared to antibacterial sutures. Taken together, these attributes indicate that AgNPr-LASE demonstrated a more balanced quality of tissue sealing and repair in diabetic and obese mice and can be used for combating local infections, that can result in poor healing in these individuals.

E-mail address: Kaushal.Rege@asu.edu (K. Rege).

^{*} Corresponding author.

1. Introduction

Wound healing is a complex process which, in healthy individuals, is characterized by four spatiotemporally regulated phases - hemostasis, inflammation, proliferation, and remodeling [1]. Several cells, including resident immune cells, fibroblasts, keratinocytes, and adipocytes in the skin regulate these phases and determine the dynamics of closure and quality of tissue repair [2,3]. Hemostasis is characterized by aggregation of platelets at the injury site, resulting in thrombosis and clot formation. The vasodilation that follows hemostasis allows influx of immune cells at the site of injury, which is a hallmark of the inflammatory phase. This phase involves recruitment of innate immune cells, including neutrophils, monocytes and resident macrophages [4] as well as cells of the adaptive immune system, including T cells, B cells, and natural killer cells [5]. Cytokines released during these events influence several processes including angiogenesis, differentiation, and re-epithelialization [6]. In later stages of healing - proliferation and remodeling - fibroblasts rapidly proliferate and deposit collagen matrix [7], ultimately leading to wound closure, recovery of biomechanical strength, and restoration of the barrier function of skin.

Approximately 350 million people worldwide suffer from diabetes [8] and nearly 25 % of these patients develop slow-healing, difficult-to-heal or intractable, chronic wounds, primarily in their lower limbs or feet [9]. Diabetic foot ulcers are a significant medical concern with 5-year survival rates that are lower than some common cancers [10]. The dysfunctional and inflamed tissue microenvironment in diabetes contributes to abnormal healing of wounds, which, over time, can develop to chronic wounds [11]. Consequently, surgical procedures in diabetic or immunocompromised individuals involve elevated risk of poor wound closure, dehiscence, infection, and scarring [12-18]. Indeed, diabetes and obesity are considered among highest risk factors for surgical site infections (SSI) [19,20], and particularly diabetes was considered as the greatest independent risk for SSI [14,21-26]. Staphylococcus aureus, isolated in approximately 23 % of infected ulcers, is a major contributing pathogen to SSIs, including in diabetic patients [27–30]. Of particular concern, methicillin-resistant S. aureus (MRSA) infections in diabetic patients significantly increased from 2003 to 2007 [31], corresponding with increasing rates of community-acquired MRSA infections in the 1990s and early 2000s [32,33]. Impaired and dysfunctional neutrophils, macrophages, and other cells of the innate immune system collectively compromise healing, tissue repair, and cosmetic outcomes in diabetic hosts, all factors that necessitate the development of novel biomedical interventions for effective skin and soft tissue repair.

Sutures and staples are commonly used to approximate and close incisional and small area wounds. Materials and processing innovations have improved mechanical strengths and sterility while essentially maintaining the basic working mechanism of these common approximation devices [34,35]. Although sutures and staples approximate adjacent tissue edges together, the noncontinuous seal together with superficial and heterogeneous tension distribution around the wound can lead to extensive scarring which can contribute to the formation of 'railroad track' scars [36,37]. Moreover, sutures are also prone to infections, do not integrate with tissue, and depending on the site, need to be subsequently removed [37–39].

Adhesives interact with tissues physically by means of ionic interactions, van der Waals interactions, and/or chemical conjugation [40, 41], resulting in strong biomaterial-tissue adhesion [42]. Synthetic adhesives, including cyanoacrylate-based glues, are used for skin sealing and lead to improved cosmetic outcomes and reduced application times when compared to sutures [43]. However, these glues are intended only for superficial use, and some formulations resulted in contact dermatitis and wound dehiscence in patients undergoing head and neck surgeries [44], which necessitates development of more effective alternatives.

Laser-activated sealing is a powerful approach for facilitating rapid tissue approximation, sealing, and repair [45,46], and we have

developed laser-activated sealants (LASE) to enhance the efficacy of this approach [47–49]. LASE consists of a photothermal converter (i.e., light-absorbing dyes or nanoparticles) embedded within a biomaterial matrix. Upon irradiation, LASE convert incident laser energy to heat thereby elevating the local temperature, which can induce structural changes in tissue proteins and the LASE. Upon annealing, LASE macromolecules are thought to interdigitate with tissue proteins resulting in rapid liquid-tight tissue sealing [45,50]. Additional advantages of LASE sealing include low and homogeneous strain throughout the injury site [51], and the ability to deliver bioactives, including antibiotics to combat surgical site infection [50]. Bioengineering of effective LASEs for healthy, as well as diabetic and obese individuals is critical for successful skin and soft tissue healing following surgical approximation and sealing.

Here, we report a comprehensive investigation into new LASEs for rapid sealing and repair of incised tissues in diabetic, obese mice, as well as immunodeficient mice, considering the significant challenges to effective healing outcomes associated with these pathologies. We developed LASEs in which copper (Cu) salt and silver nanoprisms (AgNPr) were employed as photothermal converters of near-infrared (NIR) laser energy and embedded them within matrices made from silkworm silk fibroin protein. Although our primary interest is driven by their photothermal properties [52], copper is known to demonstrate proangiogenic and antibacterial activities [53,54]. Silver nanoparticles can also have antibacterial properties, as is known for this metal, including with laser irradiation [55]. Our results show that laser sealing with bioactive LASEs can be an effective alternative approach for skin closure, and shows differential closure rate, immune response, and cosmetic outcomes compared to sutures. We fabricated antibacterial LASEs by loading AgNPr-LASE with vancomycin, which is an antibiotic drug with known efficacy against MRSA pathogens, thus resulting in the fabrication of bioactive devices with simultaneous sealing and infection control activity. Our results indicate that AgNPr-LASE loaded with vancomycin (AgNPr-Vanc-LASE) demonstrated high efficacy for combating SSIs in a MRSA challenge model in diabetic and obese mice.

2. Experimental

2.1. Materials

Bombyx mori cocoons (Mulberry Farms, CA, USA), lithium bromide (Sigma-Aldrich, MO, USA), sodium carbonate (Sigma-Aldrich, MO, USA), copper chloride dihydrate (Fisher Scientific, NJ, USA), polyvinyl pyrrolidone (PVP)-silver nanoprisms (AgNPr) in aqueous 5 mM sodium borate (nanoComposix, CA, USA), vancomycin hydrochloride (Chem-Impex International Inc., IL, USA), 3.5 kDa molecular weight cut-off dialysis bags (Spectra/Por, Spectrum Labs, CA, USA), and 4-0 black Monosof monofilament nylon sutures (Medtronic, MN, USA) were purchased from respective commercial vendors as indicated.

2.2. Extraction of silk fibroin from silkworm cocoons

Silk fibroin protein (henceforth, "silk") was enriched from *Bombyx mori* silkworm cocoons using protocols described previously [50]. Briefly, each cocoon was cut into four pieces and 10 g of these pieces were added to 4 L of boiling water containing 0.02 M Na₂CO₃ for 30 min with intermittent mixing. They were then removed and washed three times in NanopureTM water (NPW; resistivity = 18.2 M Ω cm⁻¹) for 20 min to remove excess Na₂CO₃. Silk fibers obtained from this process were dried overnight in the air. Dried fibers (7 g) were tightly packed in a glass beaker, and 28 mL of LiBr (9.3 M in NPW) were added to the beaker. The beaker was incubated at 60 °C for 4 h to dissolve the silk fibers. Dissolved silk was then dialyzed through a 3.5 kDa membrane against NPW for 72 h to remove any potential lower molecular weight contaminants. The dialysis water was changed after 0.5, 1, 2, 4, 12, 24, and 48 h. The concentration of the silk solution was determined by

drying 0.5 mL solution at 60 $^{\circ}$ C and weighing the dried silk fibroin protein. The desired concentration of silk solution was prepared by dissolving the required amount of dried silk in NPW.

2.3. Preparation of LASE Films

CuCl2•2H2O salt or PVP-AgNPr nanoparticles were added to 6 % (wt./vol.) silk fibroin solution in NPW and gently mixed on a rotary shaker for 5 min to prepare the required concentrations of silk-CuCl₂ solutions or silk-AgNPr dispersions. From this, 0.5 mL solution/dispersion was spread evenly over the surface of plastic coverslips in order to generate silk-Cu or silk-AgNPr films (\sim 22 mm \times 22 mm in dimension); the liquids were allowed to dry overnight in air at room temperature leading to the formation of LASE films. CuCl2 and AgNPr concentrations of 10 μ moles and 10 μ g per film, respectively, were used for effective photothermal conversion. For LASEs used to combat local infection, 2 mg vancomycin hydrochloride was used per film. All LASE films were sterilized using ethylene oxide treatment prior to their use in vivo. Thickness of all films was determined using Vernier calipers and verified using a micrometer. Nomenclature used for LASE films with corresponding silk, CuCl₂, AgNPr, and vancomycin concentrations along with their amounts used in vivo are listed in Table 1. The amount of the photothermal converter (CuCl2 or AgNPr) and silk used was kept the same in all mice, and this results in lower amounts per kg in db/db diabetic and obese mice, which are higher in weight compared to other strains used.

2.4. Absorbance Spectroscopy of LASE Films

Cu-LASE, AgNPr-LASE, and silk-only films were placed on lids of a 6-well plate. Absorbance spectra of all films were determined between 400 nm and 900 nm using a BioTek Synergy 2 plate reader (BioTek Instruments, VT, USA) in order to determine their light absorption properties. To determine spatial distribution of chromophores within LASE, the absorbance of films was measured at 25 individual locations in a 5×5 matrix for every film at 808 nm using the plate reader; at least three independently prepared films were used in this study.

2.5. Photothermal Characterization of LASE Films

Cu-LASE, AgNPr-LASE, and silk-only films were cut into small squares of 3 mm \times 3 mm (approximately 40 μm in thickness) and placed onto a glass slide. A hand-held 808 nm continuous wavelength near infrared (NIR) laser (LRD-0808, Laserglow Technologies, North York, Ontario, Canada), coupled with armored optical fiber with FC/PC connector (#AFF2001X, 1 m in length and 200 μm in core diameter), was irradiated over the film for 30 s and the temperature change was recorded during the on (30 s) and off (30 s) cycle (total three cycles) using a A325sc infrared camera (A325sc NIR; FLIR, Nashua, NH, USA).

2.6. Mechanical Characterization of LASE

Cu-LASE and AgNPr-LASE were cut to 20 mm × 7.5 mm (approximately 40 μm in thickness) to effectively fit in the clamps of the instruments used for mechanical analyses. To investigate changes after photothermal (laser) treatment, 20 μL of phosphate-buffered saline (PBS; NaCl: 137 mM, KCl: 2.7 mM, Na₂HPO₄: 10 mM, and K₂HPO₄: 1.8 mM; pH~7.4) was first added to a plastic slide and LASE films were placed over the saline solution. These LASE films were then irradiated with the 808 nm wavelength, hand-held laser for 2 min, which allowed the temperature to reach 65 °C (power density: 4.8 W/cm²). The films were then dried in air for about 20 min, loaded onto a TA.XT Plus Texture Analyzer instrument, and subjected to uniaxial tensile force. The speed of separation was set at 2 mm/s, and the maximum force before the film ruptured was divided by the cross-sectional area of the film (0.3 mm²) to obtain ultimate tensile strength (UTS). Young's moduli were calculated by measuring the slope of the stress-strain curves in the linear elastic region.

LASE films were cut to dimensions of 15 mm \times 10 mm and loaded between the two clamps of the Dynamic Mechanical Analysis (DMA) fixture of the Discovery HR30 rheometer (TA Instruments, DE, USA) in order to determine their rheological properties. The films were subjected to a frequency sweep from 1 Hz to 10 Hz for a strain of 0.1 %, and the storage and loss moduli were determined.

2.7. Fourier-Transform Infrared (FTIR) Spectroscopy of LASE Films

AgNPr-LASE and Cu-LASE films were irradiated with the handheld laser operated at different powers such that the temperatures reached 45, 55, 65, or 85 °C as a result of the photothermal response of these LASEs; temperatures were monitored in real time using the thermal camera. Non-irradiated LASE films were used as controls. FT-IR spectra of LASEs were acquired using a Bruker Alpha FT-IR spectrometer (Billerica, MA, USA) with a platinum ATR module utilizing OPUS software. Spectra were collected with a spectral window of 400–4000 cm⁻¹ at 4 cm⁻¹ resolution and 64 scans. To understand the compositions of different secondary structures from the FTIR spectra, a peak deconvolution analysis was conducted on the amide I region using "ylftir", a home-developed open-source Python package for deconvolutions. First, spectra were smoothed using a 9-point Savitzky-Golay method, and baseline corrected using a cubic spline along the amide I and II bands. Three peaks were fit for silk solution and silk-Cu solution and four peaks were fit to the spectra of films, where a peak at 1698 cm^{-1} was added to improve the quality of the fit. Following Urie et al. [45], we chose two Lorentzian peaks for β -sheet structures at 1618 cm⁻¹ and 1698 cm⁻¹, and two Gaussian peaks for helix/random coil at 1645 cm⁻¹ and 1678 cm⁻¹. Peak positions were allowed to vary by \pm 0.5 % with respect to wavenumber, and peak widths and amplitudes were allowed to grow to minimize the least-squares residual.

Table 1Dosages of photothermal converters (copper salt or silver nanoprisms), silk, and vancomycin (antibiotic drug) used in this study.

		CuCl ₂ in Cu-LASE	AgNPr in AgNPr-LASE and AgNPr-Vanc-LASE	Silk	Vancomycin in AgNPr-Vanc-LASE
Amount per LASE film (22 mm x 22 mm x 40 μm)		10 μmol	10 µg	30 mg	2 mg
In vivo dosage	Balb/c Balb/c SCID db/+	4.25 mg/kg	0.0025 mg/kg	150 mg/kg	
	db/db	2.125 mg/kg	0.00125 mg/kg	75 mg/kg	2.5 mg/kg

2.8. Determination of LASE Integrity in vitro

We studied the dissolution of laser-irradiated films under conditions that mimic their application in vivo. AgNPr-LASE were cut to obtain films with approximate dimensions of 20 mm \times 20 mm. LASE films were kept on a plastic slide, and PBS (40 μ L) was added on top and evenly spread to moisten the film. The film was irradiated with the 808 nm wavelength hand-held NIR laser for 5 min (4.8 W/cm²) and a temperature range of 55-65 °C reached as a consequence of the LASE photothermal response, was verified using a thermal camera (A325sc NIR; FLIR, NH, USA); this temperature range is deemed optimal for laser tissue sealing [45,46]. Following laser irradiation, the film was allowed to dry in the air for 1 h. AgNPr-LASE and silk-only films were used as controls. All films were first weighed (initial weight) and then kept at the bottom of 6-well plates. PBS (1.6 mL) was added to each well and the LASE films were allowed to dissolve for 1 min, 5 min, 15 min, 30 min, 1 h, or 2 h. The undissolved film was removed from the well using forceps, dried overnight on a plastic slide at room temperature and weighed (final weight). The dissolution of the film was calculated as:

$$\% \textit{ Dissolution} = \frac{Initial \ weight \ (mg) - Final \ weight \ (mg)}{Initial \ weight \ (mg)} \times 100$$

2.9. Vancomycin release from AgNPr-Vanc-LASE

The amount of vancomycin released from laser-irradiated (65 °C, 2 min) AgNPr-Vanc-LASE films (10 mm × 3 mm) was determined by measuring the concentration of the drug released into the supernatant using high performance liquid chromatography (HPLC). Briefly, four AgNPr-Vanc-LASE films were incubated in 500 µL PBS at room temperature for 5, 15, 30, 60, 120, and 300 min. Samples of the supernatant (400 µL) at the indicated time points were analyzed using an Agilent 1100 series HPLC (Santa Clara, CA, USA), equipped with a Raptor ARC-18, column (2.7 μ m, 150 \times 4.6 mm; Bellefonte, PA, USA) with phosphate buffer (pH 2.2) and acetonitrile (86:14 % v/v) as the mobile phase operating at 25 $^{\circ}$ C and a flow rate of 0.72 mL/min. Detection of the drug was facilitated by a diode array detector (DAD) at a wavelength of 205 nm. A calibration curve for vancomycin was generated using vancomycin standards of 25, 50, 100, and 200 µg/mL in PBS. Laser-irradiated (65 °C, power density = 4.8 W/cm², 2 min) AgNPr-LASE films without vancomycin, 1 cm × 3 mm, were used as negative controls. Silk-only films dissolved in PBS were used as the background (blanks). Considering that non-laser-irradiated LASEs dissolve rapidly and completely in aqueous media, and that laser irradiation and the concomitant photothermal response makes LASE films resistant to complete dissolution [45], we investigated the total amount of vancomycin released from non-irradiated AgNPr-LASE in PBS (500 µL) as a determinant of initial drug loading in the film; vancomycin released from the films into PBS was determined using the HPLC analyses described above.

2.10. $CuCl_2$ release from Cu-LASE

To generate the calibration curve of CuCl $_2$ in PBS, different concentrations of CuCl $_2$ standards (10 mg/mL, 5 mg/mL, 2.5 mg/mL, 1.25 mg/mL, and 0.625 mg/mL) in PBS were prepared. Addition of CuCl $_2$ in PBS led to formation of insoluble precipitate. In a 96-well plate, 150 μ L of standard and 50 μ L of 2 N HCl was added to dissolve the precipitates. The absorbance of standards was recorded at 800 nm and calibration curve was generated. PBS (150 μ L) with 50 μ L of 2 N HCl was used as a blank. Cu-LASE films (22 \times 22 mm; thickness: 40 μ m) were hydrated with 40 μ L PBS and lasered for 5 min (temperature: 55–65 °C, power density: 9.6 W/cm 2). These films were then cut into 12 pieces with scissors. Cu-LASE films, not irradiated with the laser, were also processed similarly. Next, these film pieces were incubated in PBS (300 μ L) in a 48-well plate. Supernatant (150 μ L) was withdrawn at 1 min, 5 min, 15 min, 30 min, 1 h, 2 h, and 4 h and added to a well of 96-well plate.

Any precipitated salts in the supernatant, as a consequence of reaction with PBS [56,57], were dissolved by adding 50 μ L 2 N HCl in the supernatant. The absorbance of the samples was measured at 800 nm wavelength using a plate reader.

2.11. In vivo Laser Sealing in Live Mice

Balb/c (immunocompetent), Balb/c SCID (immunodeficient mice, which lack mature B and T lymphocytes), B6.BKS(D)-Lepr db/J homozygous (db/db) (immunocompetent, diabetic and obese), and heterozygous (db/+; immunocompetent) mice were purchased from Jackson Laboratory (ME, USA) at \sim 7 weeks of age. The animals were allowed to acclimatize for at least one week and 8–12-week-old mice were used for the surgery. Equal numbers of male and female mice were used; when n = 3 mice were used in a group, at least one mouse with opposite sex was used. All procedures were approved by the Institutional Animal Care and Use Committee (IACUC) at Arizona State University.

A full-thickness incision wound model was used in Balb/c, Balb/c SCID, and db/db mice to evaluate the efficacy of LASEs in different hosts that represent different physiological conditions. Blood sugar levels of diabetic mice were determined before surgery to ensure that they exhibited the diabetic phenotype; mice with glucose levels >250 mg/dL can be considered diabetic [58,59]. The glucose levels of representative mice in our studies were 537, 305, 255, 289, 460, and 377 mg/dL (male) and 420, 244, 196, 471, 386, and 256 mg/dL (female) as determined using a glucometer (Accu-Check Aviva Plus, IN, USA). Before surgery, the mice were anesthetized by intraperitoneal (i.p.) administration of a 100 µL anesthetic cocktail containing 120 mg/kg of ketamine and 6 mg/kg of xylazine. The dorsum of the mice was shaved using clippers and then sterilized by application of 2 % chlorhexidine gluconate and 70 % ethanol three times except in case of experiments on the MRSA infection cutaneous challenge where chlorhexidine gluconate was excluded to avoid any residual antimicrobial activity because of this chemical. In MRSA challenge studies, the dorsum was treated with 70 %ethanol and PBS three times. A full-thickness incision of 1 cm length was made in the shaved and sterilized dorsal skin using sterile surgical scissors. Approximately 10 µL PBS were added to the incision to moisten it. The LASE film, cut to the size of the wound (\sim 1 cm \times 3 mm), was then placed on top of the incision and allowed to hydrate for 30-60 s. After the LASE film formed a paste, the incision was first physically approximated using forceps. The incision with LASE was then irradiated with the hand-held NIR laser for 2 min. The laser was held perpendicular to the wound in order to facilitate effective adhesion of the LASE to the tissue. The temperatures of the incision and surrounding tissue were continuously monitored using an infrared thermal camera. Based on continuous temperature feedback from the thermal camera, the laser was moved towards or away from the incision in order to ensure that the temperature remained in the range of 55-65 °C throughout the duration of the laser sealing procedure. Additionally, the handheld laser was moved in a zig-zag pattern (perpendicular to incision) rapidly to ensure that the temperature increased in a controlled manner and that the residence time at a location was minimized in order to minimize potential thermal damage.

2.12. Determination of Transepidermal Water Loss (TEWL)

Transepidermal water loss (TEWL), which is an indicator of the barrier function of skin [60,61], was determined by gently placing a VapoMeter instrument (Delfin, FL, USA) on top of the healing skin. TEWL values (in g/m^2h) were recorded from three different points along the incision, and their mean was considered as the TEWL value for the whole incision. The values for intact skin were recorded on the shaved dorsal, intact skin of mice.

2.13. Evaluation of Ultimate Tensile Strength (UTS) and Young's Modulus of Healed Skin

On day 2 post closure, skin around the incision was excised and cut to 2 cm \times 1 cm. The skin was then loaded between the clamps of the TA.XT Plus Texture Analyzer Instrument and subjected to uniaxial tensile force perpendicular to the wound until it broke into two parts. The velocity of clamp separation was 2 mm/s, and the trigger force was set to 0.01 N. The UTS value (in MPa) - defined as the maximum stress a material can withstand before failure - was obtained from the stress-strain curve. Young's modulus (MPa) is a measure of the stiffness or elasticity of the material and was determined as the slope of the stress-strain curve in the linear region.

2.14. Tissue Collection and Processing for Histology

Tissue samples containing the incision site were harvested from mice on day 2 following closure for Balb/c, Balb/c SCID, db/db, and db/+ mice and on day 7 post closure for db/db and db/db MRSA-challenged mice. All samples were stored between two foam biopsy sponges in a histology cassette. The cassettes were submerged in 10 % neutralbuffered formalin (#HT501128, Sigma Aldrich, St. Louis, MO, USA) for at least 72 h in order to fix the tissues at room temperature before further processing. The samples were dehydrated in a graded series of ethyl alcohol (40%-100 %) followed by two exchanges of xylene. Finally, the tissues were embedded in Paraplast Plus paraffin (#19217, EMS Diasum, Hatfield, PA, USA). Paraffin-embedded tissue blocks were cooled on ice and cut into 5 µm sections using an Accu-Cut® SRMTM 200 rotary microtome (Sakura Finetek USA, Torrance, CA) and collected on charged glass slides (Hareta, Springside Scientific, Durham, NC) in a floating deionized water bath (XH-1003, IHC World, Ellicott City, MD) set at 42.4 °C.

2.15. Hematoxylin and Eosin (H&E) Staining

Paraffin-embedded tissue sections on positively charged slides (AHS90-WH, Hareta Control Slides, NC, USA) were deparaffinized by incubating a loaded vertical slide rack at 60 °C for 30 min. Next, the slides were cleared in xylene and rehydrated in a graded ethanol series (100 %, 90 %, 70 %), and finally tap water. The samples were then stained by incubating the slide rack in a solution of hematoxylin (Gill No. 2, #GHS232, Sigma Aldrich, St. Louis, MO, USA) for 3 min, followed by three exchanges in tap water (for 30 s, 1 min, and 2 min) to wash excess stain. Further, the slides were quickly dipped in an acid-alcohol solution (0.3 % hydrochloric acid in 70 % ethanol) 10-12 times, washed in tap water, and then blued by submersion in ammonia water (0.2 % ammonium hydroxide in distilled water) for 30 s. Next, the slides were stained in 0.5 % eosin Y solution (#318906, Sigma Aldrich, St. Louis, MO, USA) in distilled water acidified with 0.2 % glacial acetic acid v/v for 4 min. The slides were washed in 90 % and 100 % ethanol for 2 min each followed by two washes in 100 % xylene. The slide rack was air dried at room temperature for at least an hour. After drying, the slides were mounted with Cytoseal XYL (Richard-Allan/Thermo Fisher Scientific, Kalamazoo, MI, USA) and a 1.5# coverslip. Imaging was carried out on an Olympus BX43 upright microscope equipped with an Olympus DP74 CMOS camera. The cellSens software was used to operate the microscope camera and capture the images (Olympus Corporation, Center Valley, PA, USA).

2.16. Immunohistochemistry (IHC)

Paraffin-embedded tissue sections were cut into 5 μ m-thick sections using a microtome, and the sections were collected on a positively charged glass slide. Slides were incubated at 37 °C overnight to dry. The next day, the slide rack was moved to a 60 °C dry heat oven for 1 h after which, the slides were rehydrated through a graded ethanol series and

finally tap water. After rehydration, the sections were incubated overnight at 60 °C in an epitope retrieval buffer (10 mM sodium citrate, 0.5 % Tween-20; pH 6.0). The next day, slides were washed with 1X TBST buffer (0.1 % Tween 20 in Tris-buffered saline; pH 8.4) and a hydrophobic barrier was applied around the tissue. To prevent non-specific binding of the primary antibody, the sections were blocked using 5 % bovine serum albumin (BSA) (Fisher Scientific, NJ, USA) (in TBST) for 1–2 h. Primary antibody dilutions were prepared in 5 % BSA (in TBST) using the manufacturer's protocol and internal optimizations. After blocking, the BSA solution was decanted, and primary antibody solution (1–5 μ g/mL; 90 μ L was added and overlaid with a parafilm coverslip. The slides were incubated at 4 °C overnight. The next day, the primary antibody was decanted, and the slides were washed three times with TBST. In the case of horseradish peroxidase (HRP)-conjugated secondary antibodies (Jackson ImmunoResearch, PA, USA), the slides were quenched with 3 % hydrogen peroxide (in PBS) for 15 min at room temperature. After 15 min, H₂O₂ was decanted, and the slides were washed three times with TBST. After 1:500 dilution in 5 % BSA (in TBST), secondary antibody solution (0.8 mg/mL; 200 µL) was added to each slide, and the slides were kept in the dark for approximately 1 h. Excess secondary antibody was decanted, and the slides were washed 3 times with TBST. Next, Vector ImmPACT Vector Red (for alkaline phosphatase-conjugated secondary antibodies) or Vector ImmPACT DAB (for horseradish peroxidase-conjugated secondary antibodies) substrate (Vector Laboratories, CA, USA) were used for chromogen development of the Ly6G antibody (Invitrogen, MA, USA) or Arg-1 (Arginase-1) (Cell Signaling Technology, MA, USA), CD86 (Cell Signaling Technology, MA, USA), α-SMA (α-smooth muscle actin) (Abcam, MA, USA), and CD31 (Abcam, MA, USA) antibodies, respectively. After chromogen development, the slides were counterstained with hematoxylin as described above, dehydrated, and mounted using CytoSeal XYL and a #1.5 coverslip. Similar to H&E staining, the slides were imaged using an Olympus BX43 upright microscope equipped with an Olympus DP74 CMOS camera operated by cellSens Standard software. The contrast of all the captured images was enhanced by 40 %, and the image temperature was set to 5300 K in Microsoft PowerPoint.

IHC data were quantified using FIJI software. In this approach, the number of pixels in a 20X field was counted for Ly6G, CD86, and Arg-1 markers. In brief, the collected images were opened in the FIJI software, and colors were deconvoluted using the method by Landini et al. [62] and highlighting colors with region of interest markers. Hair follicles and epidermis were manually censored from the image for Arg-1 quantification to ensure that only the signal from Arg-1+ cells were included, and that non-cellular signal was not considered. Also, a strong threshold was applied to the images to include the signal obtained only from cells. To quantify Arg-1 expression in the epidermal tongue, a region of interest (brown signal from Arg-1) on both sides of the incision was manually drawn in FIJI and the absolute area (in μm²) was measured. For α -SMA quantification, the number of α -SMA + pixels in a 20X field with highest signal were enumerated. For CD31⁺ blood vessel quantification, the cell counter function in FIJI was used, stained sections of blood vessels were manually counted, and the average of two 20X fields containing the angiogenic front next to the incision was plotted for every animal.

2.17. Evaluation of Anti-MRSA Activity of AgNPr-Vanc LASEs in vitro

LASE films (AgNPr-LASE containing 10 μg per film AgNPr and AgNPr-Vanc-LASE containing 200 μg per film vancomycin) were cut into small pieces with dimensions – ~ 1 cm $\times 3$ mm – similar to those used in live animal studies. An incision, 1 cm in length, was made in a Luria Bertani agar plate (containing 10 g/L tryptone, 5 g/L yeast extract, and 20 g/L agar from Becton Dickinson, NJ, USA and 10 g/L NaCl from Thermo Fisher Scientific, MA, USA) using a sterile inoculation loop. SECUROSORBTM suture (~ 1 cm length; AmerisourceBergen MWI Animal Health, Boise, ID, USA), AgNPr-LASE, or AgNPr-Vanc-LASE were

inserted directly in the agar plate incision using forceps (ethanol wiped and air dried). MRSA USA300 (20 μL of $OD_{600nm}=0.07)$ inoculation was performed in two ways: a) spread in a tight circle around the agar plate material-embedded incision but not directly on it or b) dropped directly only over the agar plate material-embedded incision using a micropipette. Pictures of the agar plate were collected after 1, 4, and 7 days following bacterial inoculation.

2.18. Evaluation of Anti-MRSA Activity of AgNPr-Vanc LASEs in vivo

MRSA USA300 [63] was streaked onto a mannitol salt agar (Himedia Labs, Kennett Square, PA, USA) plate containing 1 µg/mL ampicillin (Thermo Fisher Scientific, MA, USA) and incubated overnight at 37 $^{\circ}$ C. A single colony was inoculated into 3 mL of tryptic soy broth (Becton Dickinson, Franklin Lakes, NJ, USA) and incubated for 16 h at 37 °C under gentle rotation. The culture was pelleted, washed two times in sterile 0.9 % saline solution, and the absorbance at 600 nm was adjusted to 0.16. This suspension, used for infection studies, was kept on ice until use. Methods for skin incision, suturing and LASE application were similar to those described previously in the 'In vivo laser sealing in live mice' section. In these studies, the laser irradiation time was divided into two durations of 1 min each. After the first minute, the mouse was rotated by 180° along the spine, and laser irradiation was performed for another minute. This modified approach was used to ensure that all portions of the incision received effective laser administration and to minimize any probability of dehiscence because these studies involved a subsequent cutaneous MRSA inoculum challenge.

Following suture closure/LASE sealing, individually housed mice were transferred to an ABSL-2 facility, carefully placed inside a biosafety cabinet and arranged to ensure the dorsal incision site was level. MRSA infection-ready inoculum (approximately 5 \times 10^5 CFU in 10 $\mu L)$ was evenly applied along the incision site using a micropipette. The mice were monitored until the infection volume dried. Skin tissue from the infection control mice was harvested 1 h post MRSA administration in order to determine the initial MRSA load in these studies. For the remaining groups, pictures of the incision site were taken throughout the duration of the infection. On day 7, the remaining groups were humanely euthanized via CO₂ asphyxiation. Immediately after the mice were euthanized, incision sites, approximately 2 cm \times 1 cm section, were excised and stored at 4 °C for 0.5-2 h. Skin samples were radially divided (perpendicular to the incision), the bottom tissue half (nearest the mouse tail) was weighed (60-100 mg), placed into a microcentrifuge tube with 400 µL of saline and five 1.6 mm stainless steel beads (Next Advance, Troy, NY, USA). The other half was used for histological analyses performed as described earlier. The tissue was homogenized using a Bullet Blender Storm 24 (Next Advance, Troy, NY, USA) at a speed setting of 6 for a total of 10 min. The homogenate was serially diluted in saline and spot plated (5 µL) in triplicate onto mannitol salt agar + ampicillin (1 μ g/mL) plates. Agar plates were incubated at 37 °C for 24 h for CFU enumeration. MRSA bacterial loads were reported as CFU per total skin sample analyzed (60-100 mg) per mouse. The groups evaluated in this study were: nylon sutures alone, nylon sutures + vancomycin ("Nylon-Vanc"), antibacterial (containing chlorhexidine diacetate) SECUROSORBTM PLUS sutures (AmerisourceBergen MWI Animal Health, Boise, ID, USA), AgNPr-LASE films, and AgNPr-Vanc-LASE films in which 2 mg vancomycin was incorporated in 30 mg LASE film (vancomycin delivered to mice; ~2.5 mg/kg). The vancomycin loaded in each film for in vivo studies was increased 10 times compared to in vitro studies because 200 µg vancomycin per film dose which was found effective in in vitro studies - was found to be inadequate for inhibiting MRSA growth in vivo (data not shown). Vancomycinloaded LASEs were prepared using methods similar to those described above with the exception that the antibiotic was incorporated during the film preparation process.

2.19. Statistical Analyses

At least three independent experiments were carried out in all cases, and data are plotted as the mean \pm standard error of mean (SEM) or standard deviation (SD). Statistical analyses were performed using one-way or two-way analysis of variance (ANOVA) followed by post-hoc analysis using Fisher's least significant difference (LSD) method.

3. Results and discussion

Immunocompromised, diabetic, and obese patients experience several challenges in wound healing and tissue repair, including slow healing, poor quality of repair, and opportunistic infections [17]. To overcome these challenges, new strategies that can improve the efficacy of wound closure and quality of tissue repair are necessary. Here, we generated laser-activated sealants to facilitate rapid sealing of full-thickness incisional wounds in immunocompromised and diabetic, obese mice. Given their proangiogenic and/or antibacterial bioactivities, copper salts and silver nanoprisms were evaluated as photothermal converters in LASEs. Cu-LASE and AgNPr-LASEs were fabricated by a method described in Fig. 1a, characterized, and evaluated for sealing full thickness incisional wounds in healthy Balb/c, immunodeficient Balb/c SCID, diabetic and obese db/db mice as well as their non-diabetic db/+ littermates. Balb/c SCID mice possess homozygous severe combined immune deficiency (SCID) spontaneous mutation which is characterized by absence of functional T cells and B cells, lymphopenia, and hypogammaglobulinemia [64]. Commonly used in diabetic wound healing studies [65,66], db/db mice possess homozygous mutation in leptin receptor, which makes them polyphagic, polydipsic, and polyuric. Mice heterozygous for this mutation (db/+) were also used as controls for evaluating LASEs.

3.1. Spectroscopic Characterization of LASEs

Absorbance spectroscopy studies showed that Cu-LASEs and AgNPr-LASEs (Fig. 1b) absorb light in the near infrared (NIR) region (>750 nm; Fig. 1c), which makes them suitable for photothermal sealing of tissues using a laser set at a wavelength of 808 nm. In AgNPr-LASEs, a red-shift in the peak wavelength occurred when the nanoparticles were embedded inside the silk solution and dried during film fabrication. Nevertheless, the films demonstrated appreciable light absorption at 808 nm, which is required for a robust photothermal response in the NIR region. Spatial distribution of Cu and AgNPr, determined using absorbance measurements at 808 nm different locations in individual LASE films, indicated nearly uniform distribution of copper ions in the films and some heterogeneity in case of AgNPr, likely because of differential transport of these nanoparticles in the biomaterial (Fig. S1, Supporting Information section). Silk-only films, without any light absorbing species (Cu or AgNPr), did not absorb significantly in the range of 400-990 nm (Fig. 1c and Fig. S1, Supporting Information section).

3.2. Photothermal Characterization of LASEs

Upon laser irradiation, both Cu-LASE and AgNPr-LASE films demonstrate a rapid increase in temperature as recorded by a thermal camera (Fig. 1d and e). At a laser power density of 4.8 W/cm², AgNPr-LASE reached a temperature range of 55–65 °C in only 10 s, which indicated a rapid photothermal response of these films. Similarly, Cu-LASE reached the same temperature range in 10 s at power density of 9.6 W/cm²; use of higher amounts of copper can result in use of lower laser powers. The rapid photothermal response is critical to maintaining stable temperatures while using a low residence time of the laser during tissue sealing. Heating and cooling profiles in Fig. 1d and e also demonstrate the reversibility of the photothermal response across multiple cycles of laser application. In absence of the light-absorbing species (chromophores), such as copper salts or AgNPr, silk films did not

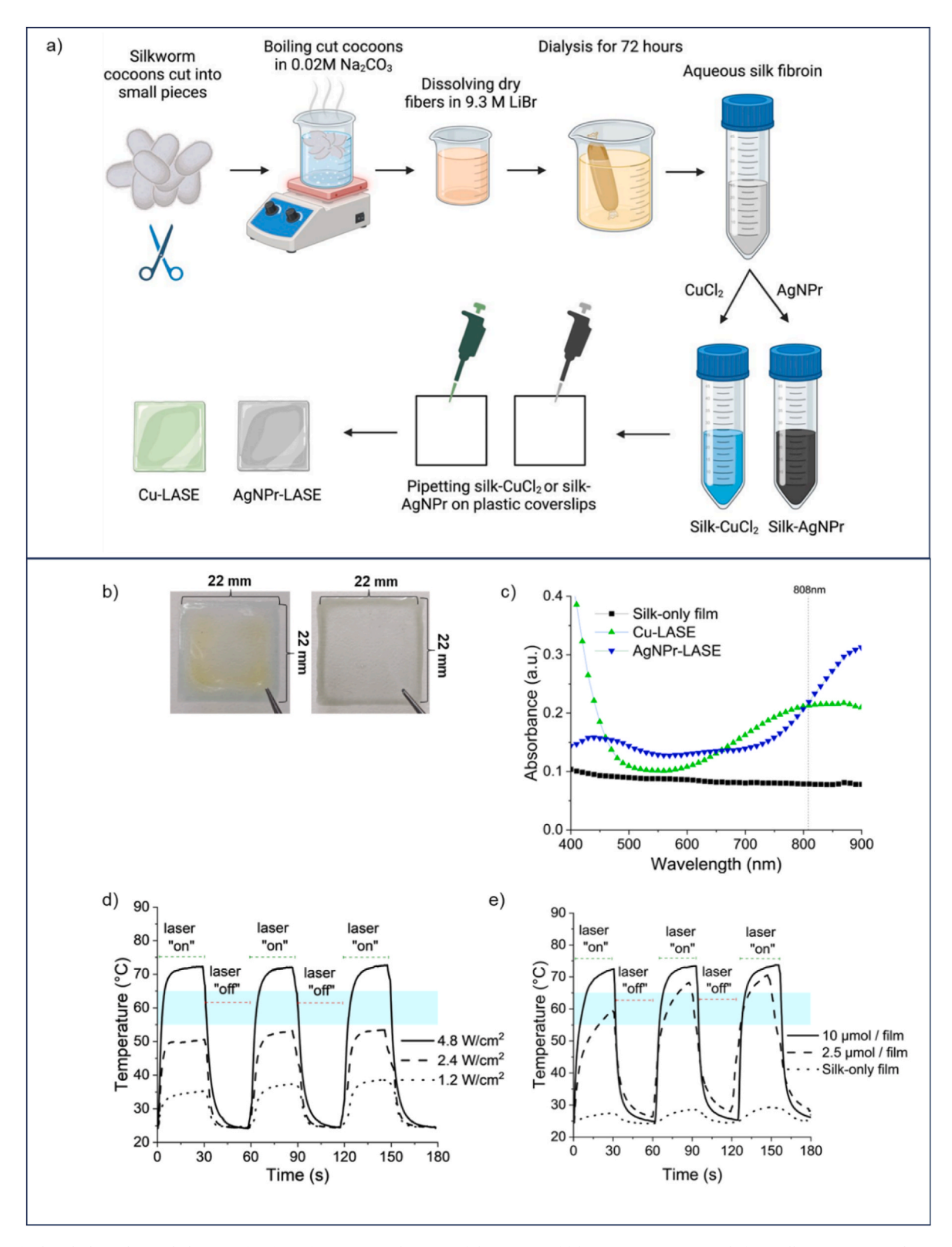


Fig. 1. Optical and photothermal characterization of LASEs. a) Schematic of the process of fabricating LASE materials from silkworm cocoons. b) Digital images of Cu-LASE and AgNPr-LASE films prepared using solvent-evaporation method. c) Visible light absorbance spectra of LASEs indicate absorption in NIR region (~750–900 nm). d) Photothermal response curves of AgNPr-LASEs as a function of power density for a hand-held 808 nm laser; AgNPr: 10 µg per film. e) Photothermal response curves of Cu-LASEs as a function of CuCl₂ concentration at a power density of 9.6 W/cm² for the hand-held 808 nm laser. The horizontal light blue-colored band in (c) and (d) show the optimal temperature range (~55–65°C) for tissue sealing [46]. (For interpretation of the references to color in this figure legend, the reader is referred to the Web version of this article.)

demonstrate absorption of NIR light and therefore a significant rise in temperature was not observed upon NIR laser irradiation (Fig. 1e).

3.3. Physicochemical characterization and stability of LASEs

Ultimate tensile strength (UTS) studies indicated that the strength of the dry non-laser-irradiated ('unlasered') films was ${\sim}62\pm16$ MPa for Cu-LASEs and \sim 58 \pm 9.5 MPa for AgNPr-LASEs, indicating no significant differences between the two LASEs. UTS for lasered films was ~ 52 \pm 10 MPa for Cu-LASEs and \sim 43 \pm 8 MPa for AgNPr-LASE (Fig. 2a). Heating of silk films, including by means of photothermal activation using lasers, can cause changes in their secondary structure, which in turn, can make these films resistant to dissolution in aqueous solvent [67]. AgNPr-LASE films, irradiated with the NIR laser for 5 min (temperature: ~65 °C), lost approximately 55 % of their original mass in PBS within 1 min of incubation (Fig. 2b). This extent of dissolution remained constant for at least 2 h. On the contrary, unlasered AgNPr-LASE and silk-only films completely dissolved within 1 min of incubating in PBS (Fig. 2b). These data indicate that laser-irradiated films partially dissolve to form pastes while also maintaining some of the original mass. Thus, laser irradiation times and durations can be used to modulate the dissolution of films, thereby controlling their morphology.

Laser irradiation also influenced the release of $CuCl_2$ in PBS from Cu-LASE films; release of $CuCl_2$ was detected using light absorption spectroscopy. Addition of PBS facilitated release of Cu^{2+} ions from Cu-LASE

and immediately turned the solution turbid, likely because of the formation of $\text{Cu}_3(\text{PO}_4)_2$ precipitate [56,57]; this precipitate formation was seen when PBS was added to a solution of CuCl_2 . This precipitate was dissolved in 2 N HCl (3:1 v/v) to generate a calibration curve for CuCl_2 and quantify Cu^{2+} ions released from LASE films. In PBS, 50 ± 12 % of initially loaded CuCl_2 was released from laser-irradiated films compared to 57 ± 9 % from non-laser-irradiated Cu-LASE films (Fig. S2, Supporting Information section) within 15 min of incubation. In 1 h, the release increased to 66 ± 13 % from lasered films compared to 80 ± 10 % from unlasered films (Fig. S2, Supporting Information section). It can be expected that the kinetics of release of Cu^{2+} ions and precipitate formation in live animals differ significantly from those in PBS and that these species might induce differential tissue responses, including immune responses.

We also investigated potential changes in the secondary structure for unlasered and lasered Cu-LASEs and AgNPr-LASEs using FTIR spectroscopy; examples of deconvolution of AgNPr-LASE and Cu-LASE FTIR spectra are shown in Fig. S3, Supporting Information section. LASE films heated at 65 °C for 2 min in a hydrated condition represented the temperature range considered optimal for laser sealing *in vivo*. Inclusion of bivalent ions including Ca²⁺, Cu²⁺, and Mg²⁺ is known to induce structural changes in silk [68,69]. In our hands, silk-CuCl₂ solution possessed similar β -sheet content to that of silk (fibroin) in solution under the conditions investigated (Fig. 2c). The solvent evaporation and drying process, used for film formation, was not sufficient to produce

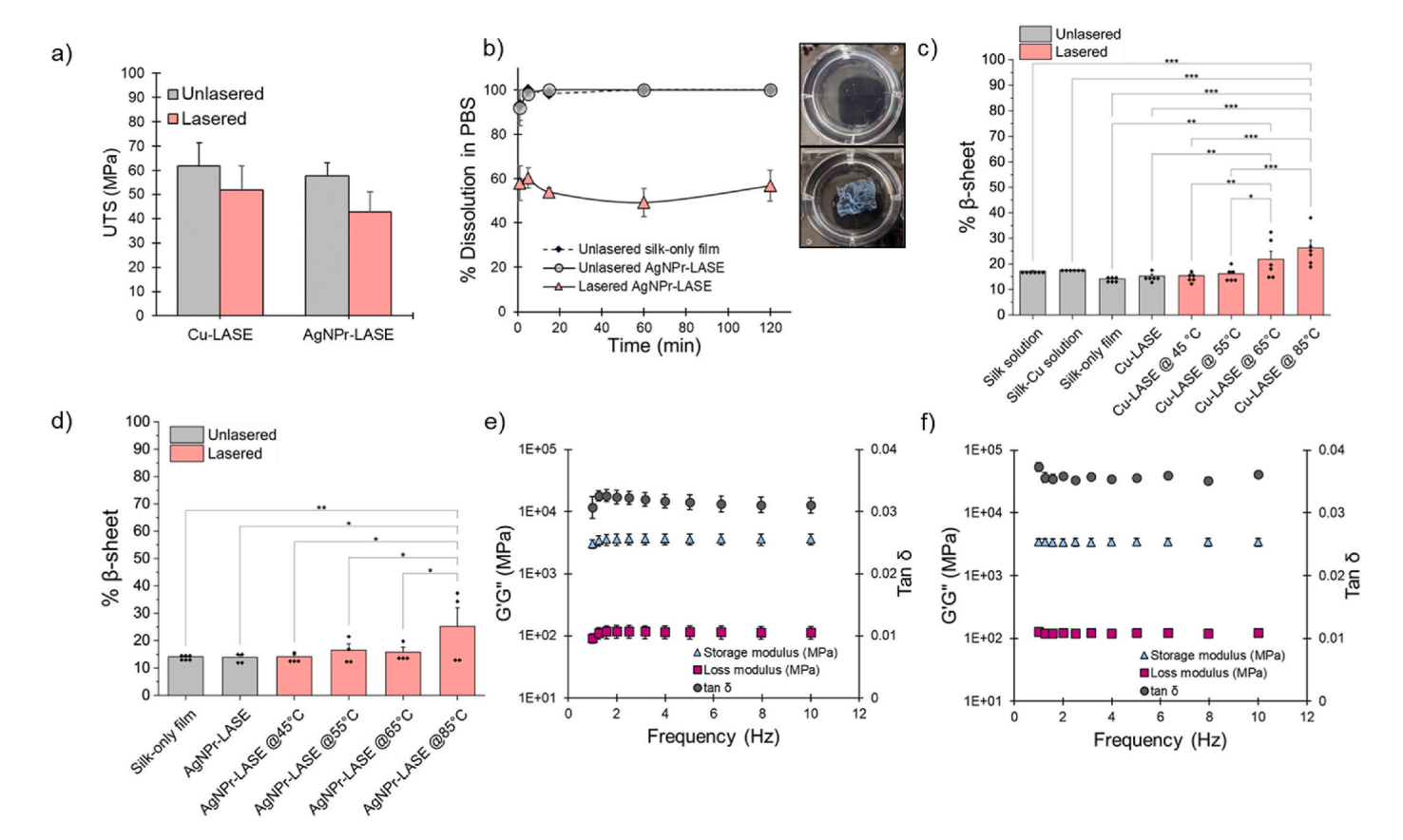


Fig. 2. Physicochemical characterization of LASE films. a) Ultimate tensile strength (UTS) of Cu-LASE and AgNPr-LASE before and after laser irradiation (2 min, 4.8 W/cm²; n = 3). The differences in the means were not statistically significant. b) Dissolution of AgNPr-LASE in PBS before and after laser irradiation (4.8 W/cm²; n = 3). Inset: digital pictures of AgNPr-LASE submerged in PBS for 5 min; top: non-laser irradiated ('unlasered') AgNPr-LASE and bottom: laser-irradiated AgNPr-LASE. c) β-sheet content of solutions and LASE films as determined by deconvolution of FTIR spectra, before and after laser irradiation, which leads to the different temperatures indicated (n = 6); the control 'Cu-LASE' condition indicates β-sheet content of these unlasered films, which were hydrated with PBS. d) β-sheet content of AgNPr-LASE films as determined by deconvolution of FTIR spectra, before and after laser irradiation (4.8 W/cm², 2 min; n = 4), which leads to the different temperatures indicated; the control 'AgNPr-LASE' condition indicates β-sheet content of these unlasered films hydrated with PBS. One-way ANOVA followed by Fisher's LSD was used to identify the significantly different groups in panels c and d. *p < 0.05; **p < 0.01; ***p < 0.001. e) Dynamic mechanical analysis (DMA) of dry, unlasered Cu-LASE (n = 4) and f) AgNPr-LASE (n = 3) after being subjected to frequency sweep between 1 Hz and 10 Hz at 0.1% strain.

significant changes in the secondary structure of the silk protein (Fig. 2c). The β -sheet content of silk-based LASEs was $\sim\!20{\text -}30$ % after photothermal treatment at 55–65 °C, which is the optimal temperature range for laser sealing of tissues. In Cu-LASE, photothermal treatment at 65 °C was sufficient to produce a significant difference in the β -sheet content compared to unlasered films (Fig. 2c). However, the β -sheet content in AgNPr-LASE at $\sim\!65$ °C was not significantly different from that of unlasered AgNPr-LASEs; the difference in β -sheet content between lasered and unlasered films was only observed when the LASEs were laser-irradiated to reach 85 °C (Fig. 2d). These results indicate that as determined by FT-IR analyses, laser irradiation did not cause significant shifts in β -sheet content in AgNPr-LASE for temperatures relevant to laser sealing and that differences in dissolution are likely due to other microstructural reorganizations in silk.

The storage and loss moduli of a material are indicative of its viscoelastic properties. Unlasered Cu-LASE and AgNPr-LASE films exhibited a higher storage modulus (G' from 10^3 - 10^4 MPa) than loss modulus ($G'' \sim 10^2$ MPa) when subjected to 0.1 % strain between 1 and 10 Hz of frequency sweep (Fig. 2 e, f). The low value of tan (δ), determined as the ratio of loss to storage modulus, indicates that LASE films are elastic in nature. For comparison, the storage modulus (G') value of full-thickness human skin is in the range of 10^2 - 10^3 MPa, and the loss modulus (G'') value is $\sim 10^2$ MPa for a frequency sweep between 1 and 10 rad/s (0.16 Hz–1.6 Hz) at 0.5 % strain [70]. These results indicate that LASE films are elastic and are suitable for applications in skin sealing and repair.

3.4. LASE-mediated Skin Sealing In Vivo

An 808 nm NIR hand-held laser was used to irradiate LASEs to facilitate skin sealing and repair in the different strains of mice used in the current study. Laser operation was carried out such that temperatures ranged between 50 °C and 65 °C. The average temperature for the entire duration of 2 min of laser activation of LASEs in Balb/c mice was $\sim\!59$ °C for Cu-LASE and $\sim\!56$ °C for AgNPr-LASE. Recovery of the barrier function of skin in live mice was determined using transepidermal water loss (TEWL) measurements, which indicate the loss of water vapor through the epidermis and is therefore reflective of its integrity.

LASE materials kept the incisions closed in all species of mice for a period of at least 2-days post closure and for 7-days in db/db mice for which longer durations were tested (Fig. 3 a-d). On day 2 post closure, Balb/c, db/db, and db/+ incisions closed with Cu-LASE and AgNPr-LASE showed similar TEWL values as those of sutures (Fig. 3e–g, h), indicating similar efficacies in restoration of barrier function in all cases. In Balb/c SCID mice, the Cu-LASE group had significantly higher TEWL values than the AgNPr-LASE group (Fig. 3f), indicating lower recovery of barrier function in case of the former.

We observed that TEWL values of incisions closed with sutures progressively decreased and became comparable to intact skin by day 7 in db/db mice (Fig. 3j). On the other hand, incisions closed with LASE exhibited similar TEWL values from day 2 to day 7, and Cu-LASE demonstrated higher values than those with AgNPr-LASEs (Fig. 3j). This can be a result of a slowly recovering epidermal layer because of the photothermal treatment and presence of the LASE biomaterial in between the wound edges. As the incision heals further, we expect to observe a further decrease in TEWL of the skin in case of incisions closed with LASEs.

To investigate early biomechanical recovery, indicative of the kinetics of tissue repair, skin tissues were excised along with the incision on day 2 post-closure, and ultimate tensile strength (UTS) of healed incisions were determined. Incisions closed with sutures in db/db mice did not heal substantially, and the healed tissue appeared fragile. In Balb/c mice, AgNPr-LASE demonstrated enhanced mechanical recovery (30 % of intact skin) compared to Cu-LASE (14 % of intact skin) and sutured (14 % of intact skin) incisions (Fig. 4a), but in

immunocompromised Balb/c SCID and db/+ mice, LASE-treated incisions had comparable UTS values to sutures (Fig. 4b and d). In db/db mice, incisions closed with AgNPr-LASEs and Cu-LASEs exhibited significantly higher UTS (17 % of intact skin) values when compared to those closed with nylon sutures (9 % of intact skin; Fig. 4c), indicating enhanced biomechanical recovery. Young's modulus measures the stiffness of the material, and AgNPr-LASE treatment in Balb/c mice significantly increased the stiffness of skin compared to other groups (Fig. 4e). The Young's modulus was equally restored among the treatment groups in other three species (Fig. 4 f-h). It is likely that presence of the LASE in the wound contributes to the higher biomechanical recovery seen for the tissue. Of key importance, LASEs, particularly those using AgNPr, can seal skin in diabetic mice and promote restoration of the biomechanical properties of the tissue.

3.5. Histology and Immunohistochemistry

H&E staining of skin tissue harvested on day 2 indicated that the gap between the wound, including epidermal edges, was covered by LASE (Fig. 5). The LASE biomaterial appeared to integrate well with the dermis, provided a continuous matrix that fills the space in the wound site, and thus likely acted as a barrier (Fig. 5a; LASE boundary illustrated by dark green perimeter for Cu-LASE in db/db mice). Physical trauma caused by sutures led to the formation of a scab, which was sparsely visible in LASE-treated incisions (Fig. 5a); LASEs themselves occupied the region inside the incision. By day 7, this scab was pushed out of the wound (Fig. 5f) and LASE still occupied the region between the two tissue edges which demonstrates its adhesive strength with the tissue. Strong adhesion of the LASE with the tissue, facilitated by photothermal activity and elevated temperatures, may reduce efficacy of epidermal gap closure but can reduce mechanical stress on the incision by covering the entire region.

On day 2 post closure, incisions sealed with AgNPr-LASEs did not demonstrate a statistically significant epidermal gap from those closed with sutures, indicating comparable performance. However, incisions sealed with Cu-LASEs had a significantly higher epidermal gap compared to those approximated with sutures in all species of mice on day 2 (Fig. 5b–e), likely because of the local toxicity of cupric ions [71]. The doses of cupric ions used in this study were 2.125-4.25 mg/kg, significantly lower than 360-640 mg/kg, which was reported to be the systemic acute toxicity dose in rats [72,73]. However, considering the relatively low hydration which obviates dilution at the incision site in the skin, we posit that the localized concentration of cupric ions may result in some toxicity to the tissue. The epidermal gap in suture-closed incisions decreased over time and reepithelialization was found to be complete by day 7 in db/db mice (Fig. 5f and g). On day 7, the epidermal gap in incisions closed with LASE did not significantly decrease compared to day 2 in db/db mice, likely because time needed for recovery of the underlying tissue from the photothermal treatment and persistence of the LASE, which filled the gap between the two edges of the incision during the duration of this study.

Biomechanical recovery (UTS; Fig. 4) indicated some benefit of LASE sealing in the initial phase of healing compared to sutures in db/db diabetic and obese mice. We therefore further investigated tissue and immune responses to LASE sealing and suturing in these mice using immunohistochemistry (IHC) on day 2 post closure. Ly6G + cells (neutrophils) appeared to swarm to the wound site closed with Cu-LASEs (Fig. 6a). These cells were found in greater numbers in Cu-LASE treated incisions compared to incisions sealed with AgNPr-LASE (p=0.0002) or approximated with nylon sutures (p=0.0208) (Fig. 6b), likely because of the diffusion of copper ions further away from the immediate vicinity of the incision bed. In Cu-LASE treated wounds, neutrophils were found to localize at a distance (1–1.5 mm) away from the incision, resulting in a neutrophil-depleted zone of about 2 mm around the wound bed (Fig. 6a–c). This finding indicates that either copper ions inhibit the migration of neutrophils or demonstrate toxicity towards these cells in

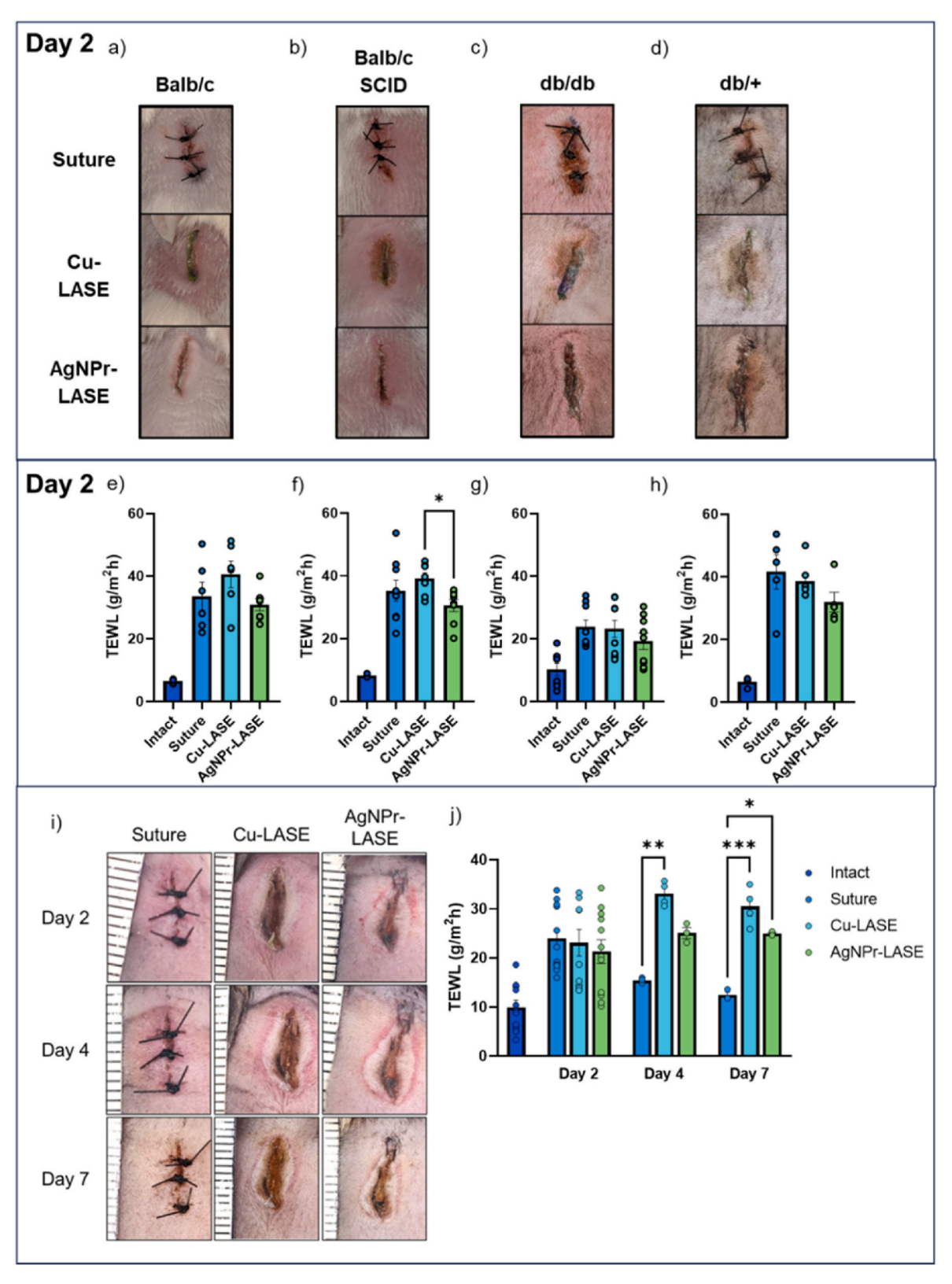


Fig. 3. Barrier function restoration efficacies of Cu-LASEs and AgNPr-LASEs compared to sutures in live Balb/c, Balb/c SCID, db/db (diabetic and obese), and db/+ (littermate) mice. a, b, c, d) Representative digital images of sealed incisions day 2 post closure in Balb/c, Balb/c SCID, db/db, and db/+ mice closed with sutures, Cu-LASE, and AgNPr-LASE. e, f, g, h) Transepidermal water loss (TEWL) for incisions closed with sutures, Cu-LASEs, or AgNPr-LASEs in Balb/c, Balb/c SCID, db/db, and db/+ mice on day 2 post closure. One-way ANOVA followed by Fisher's LSD was used to identify the significantly different groups in panels. i) Digital images of skin sections closed with sutures, Cu-LASE, and AgNPr-LASE over 7 days. j) TEWL of skin incisions closed with sutures, Cu-LASE, and AgNPr-LASE over 7 days. Two-way ANOVA followed by Fisher's LSD was used to identify the significantly different groups in panels. *p < 0.05; **p < 0.01; ***p < 0.001.

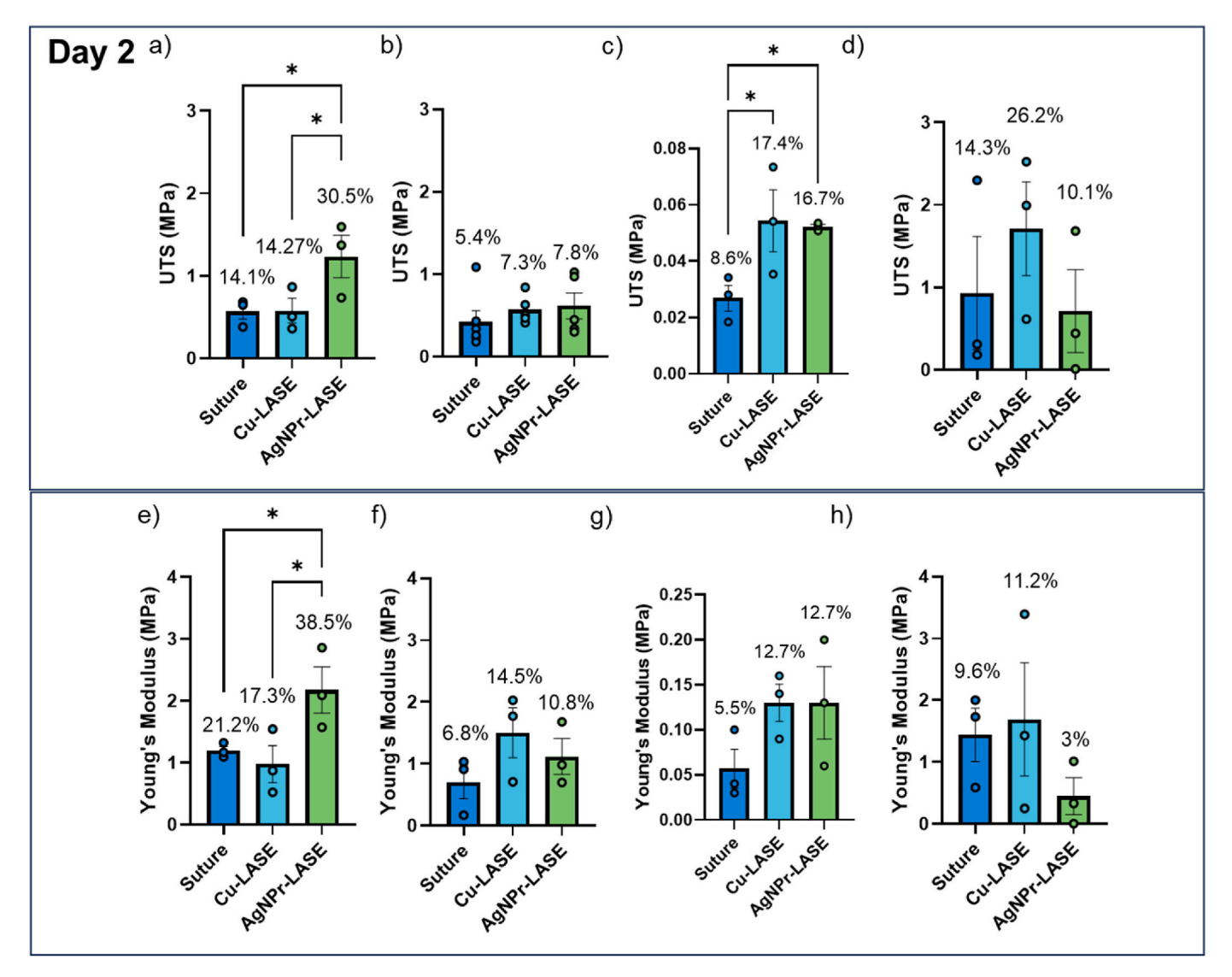


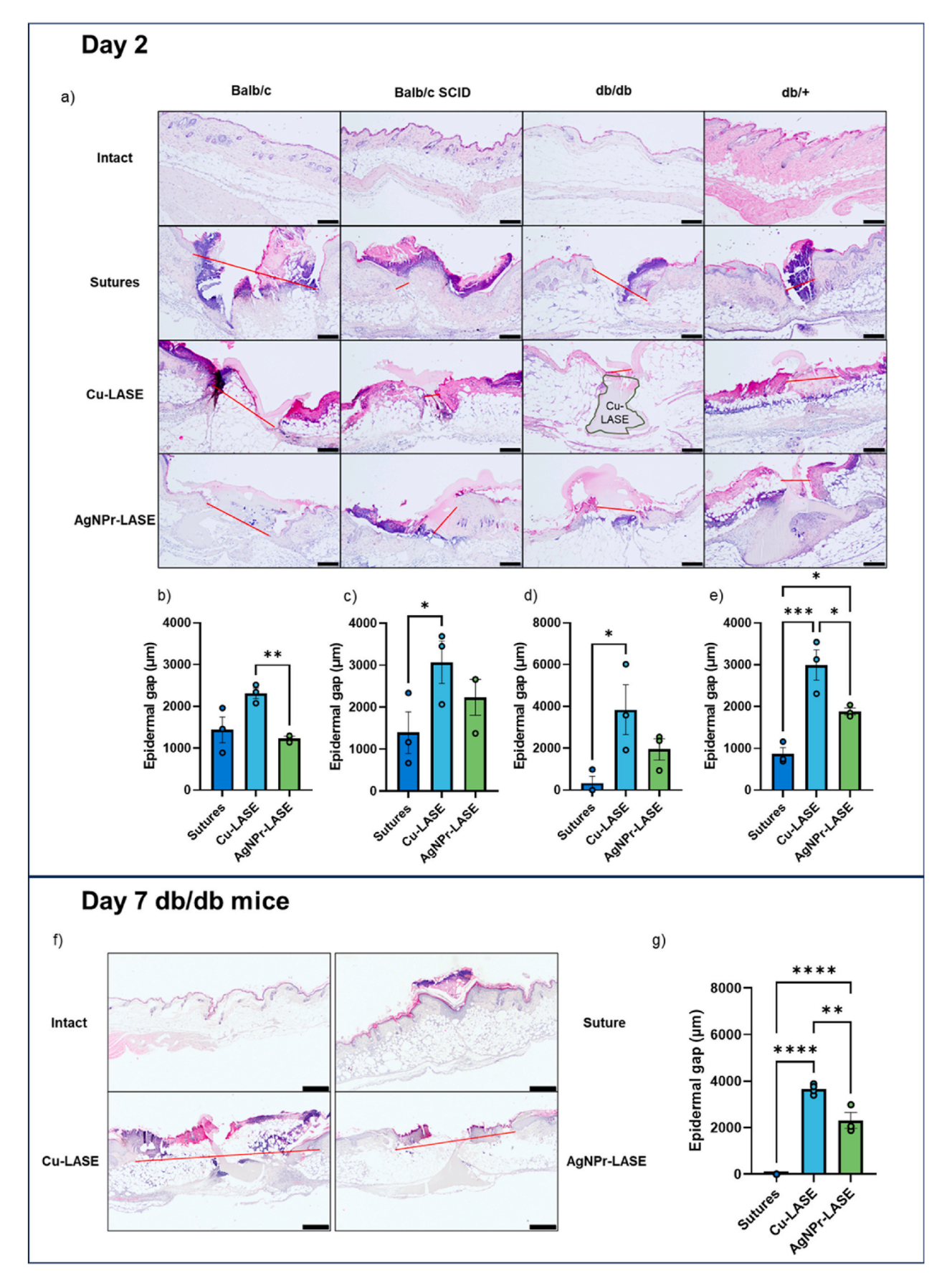
Fig. 4. Biomechanical restoration efficacies of Cu-LASEs and AgNPr-LASEs compared to sutures in live Balb/c, Balb/c SCID, db/db (diabetic and obese), and db/+ (littermate) mice on day 2 post closure. a, b, c, d) Ultimate tensile strength (UTS) and e, f, g, h) Young's modulus of healing skin on day 2 for incisions closed with sutures, Cu-LASEs, or AgNPr-LASEs in Balb/c, Balb/c SCID, db/db, and db/+ mice, respectively. Numbers above the bars represent % UTS or Young's modulus recovery of healing skin with respect to intact skin. One-way ANOVA followed by Fisher's LSD was used to identify the significantly different groups in panels. *p < 0.05.

the skin tissue under the conditions employed in this study. We reason this is likely because of copper ion toxicity at concentrations $>1~\mu g/mL$ for neutrophils isolated from mice [74]. This peculiar neutrophil-dense region, which was formed on both sides of the incision, was not observed in case of sutures or AgNPr-LASEs or in a previous study with indocyanine green (ICG)-LASE [75], which indicated that this phenomenon was likely specific to copper.

Incisions closed with AgNPr-LASEs showed significantly decreased neutrophil localization at the wound site in db/db mice, even when compared to sutures (p=0.0031; Fig. 6b) on day 2 post closure. Levels of total neutrophils for AgNPr-LASEs were significantly lower than those with Cu-LASEs and sutures (wound bed). This lower inflammation associated with AgNPr-LASEs compared to the other approximation devices could be significant for application in chronically inflamed wound microenvironments, such as in diabetic skin. This observation is consistent with our previously published results with ICG-LASE which also resulted in reduced neutrophil activity around the wound on day 2 post closure compared to sutures [75]. Additionally, in case of AgNPr-LASE-closed and suture-closed incisions, most neutrophils were localized inside the wound bed and not in an enriched zone away from

the incision site (Fig. 6c), as was seen with Cu-LASEs (Fig. 6c). In incisions approximated with sutures, neutrophils were mostly observed in the granulation tissue, and the neutrophil presence was higher than in AgNPr-LASE treated incisions (Fig. 6c).

CD86-positive or pro-inflammatory 'M1' macrophages were minimally present in the wound bed or around the periphery in all groups tested (Fig. 7a). Arginase (Arg)-1 positive macrophages are conventionally considered as 'M2' or pro-resolution macrophages that promote wound healing and tissue fibrosis by locally depleting L-arginine [76]. Arg-1+ macrophages were present in significantly higher numbers in wounds sealed with Cu-LASEs compared to those sealed with sutures (p = 0.046). However, differences in Arg-1+ levels were not statistically significant between Cu-LASEs and AgNPr-LASEs (Fig. 7b; p = 0.108). In addition, day 2 post-closure could also mark the beginning of resolution of inflammation following incisional wounding in mice. A higher proportion of Arg-1+ M2 macrophages compared to CD86⁺ M1 macrophages (Fig. 7c) indicate likely transition of the healing towards resolution of inflammation. Spatial analysis of serial sections revealed that the localization of Arg-1+ macrophages was proximal to neutrophilic localization and distal to the Cu-LASE-treated incisions as shown



(caption on next page)

Fig. 5. Hematoxylin and Eosin (H&E) staining of healed skin tissues of Balb/c, Balb/c SCID, and db/db mice on day 2 and day 7 post-surgical closure. a) Representative H&E images for incisional wounds closed with Cu-LASE, AgNPr-LASE, sutures, and intact skin in Balb/c, Balb/c SCID, db/db, and db/+ mice 2 days post-surgical closure. Red lines indicate dermal discontinuity, and the outline in case of the db/db mice shows the Cu-LASE in the tissue; scale bar: 200 μ m b, c, d, e) Quantification of epidermal gap in Balb/c, Balb/c SCID, db/db, and db/+ mice, respectively. F) Representative H&E images for incisional wounds closed with Cu-LASE, AgNPr-LASE, sutures, and intact skin in db/db mice 7 days post closure. Red lines indicate dermal discontinuity in incisions closed with LASE, which filled the gap in the incisional wound. Scale bar: 500 μ m. One-way ANOVA followed by Fisher's LSD was used to identify the statistically significant different groups in panels. *p < 0.05; **p < 0.01; ****p < 0.001; ****p < 0.0001. (For interpretation of the references to color in this figure legend, the reader is referred to the Web version of this article.)

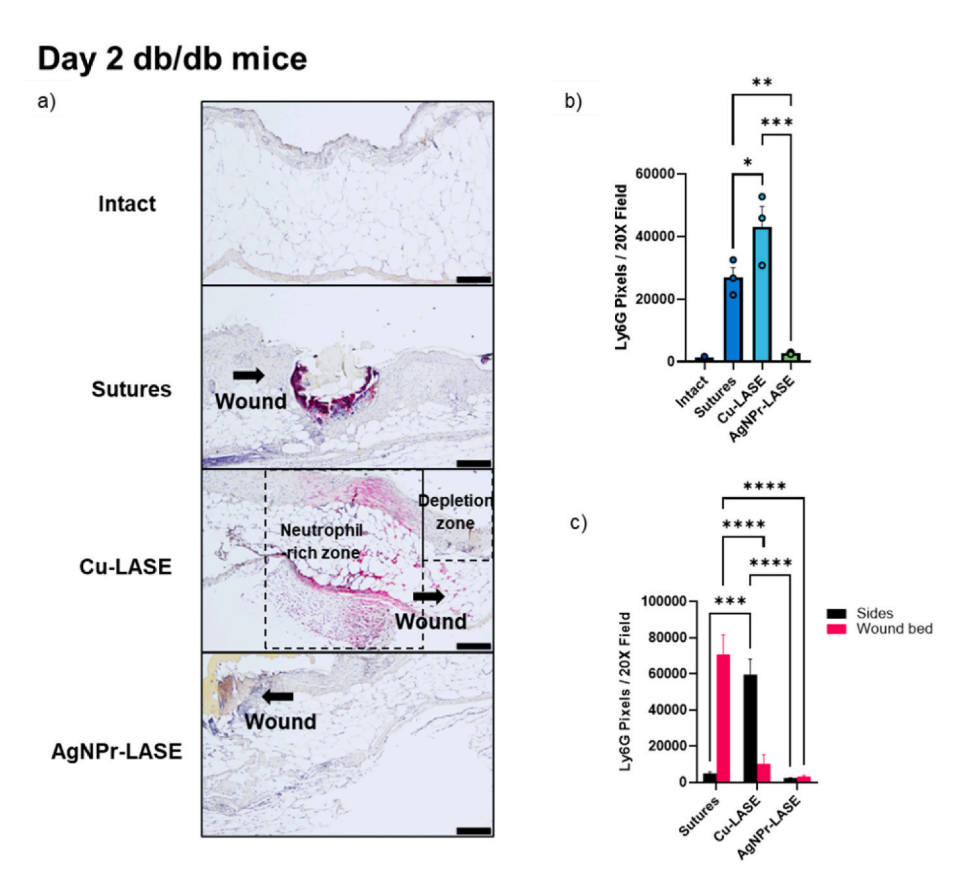


Fig. 6. Neutrophil activation and infiltration in the incisional wound bed on day 2 following LASE sealing or suturing in db/db mice a) Digital images of skin sections closed with Cu-LASE, AgNPr-LASE, or sutures compared to intact skin stained for Ly6G + cells (neutrophils) in red. Black arrows indicate the location of the incisional wound. Scale bar: 200 μ m. b) Quantitation of number of Ly6G + pixels in db/db mice wounds. c) Localization of Ly6G + pixels in the wound bed and at the wound periphery (depletion zone periphery in Cu-LASE group). One-way ANOVA followed by Fisher's LSD was used to identify the significantly different groups in panels. *p < 0.05; **p < 0.01; ***p < 0.001; ****p < 0.0001. (For interpretation of the references to color in this figure legend, the reader is referred to the Web version of this article.)

by the schematic in Fig. 7d. Taken together, the macrophage and neutrophil results indicate that AgNPr-LASE approach directs the wound towards a more pro-resolution phenotype by day 2 post-closure response, compared to the other approximation methods.

Fig. 7d shows a schematic that integrates the immune cell response to sutures and LASEs on day 2 post closure. Cu-LASEs demonstrated a depletion zone close to the wound bed in which the presence of immune cells was largely absent, likely because of the local toxicity of copper ions that diffuse into the skin from the LASE. The tissue proximal to this zone was highly enriched in neutrophils and macrophages, indicating the strong response evoked by Cu-LASEs. Suturing promoted a strong neutrophil response in the wound bed, with a concomitant peripheral M2 macrophage response. In contrast, AgNPr-LASEs demonstrated a much lower neutrophil and macrophage response in the skin tissue, indicating an overall low or muted immune response.

In tissues harvested on day 7 post-closure, we observed an increased number of neutrophils in Cu-LASE compared to sutures and AgNPr-LASE and presence of neutrophil debris around the Cu-LASE (Fig. 8a). The depletion zone observed on day 2 appeared to be displaced from the

healing skin and it is likely that it is discarded as scab over time. Most of Ly6G stained regions in case of Cu-LASE were not associated with cells, which indicated presence of neutrophil debris. A large number of neutrophils recruited around the Cu-LASE on day 2 were likely affected by copper ions released, further supporting potential toxicity of copper ions to neutrophils. The presence of some viable neutrophils on day 7 might also suggest persistent inflammation in incisions closed with Cu-LASE in db/db mice. In case of incisions closed using sutures, neutrophils were primarily localized in the scab, and some were observed in the healing tissue on day 7, much like what was observed on day 2. As with Cu-LASE, presence of neutrophils on day 7 may suggest some persistent inflammation. AgNPr-LASE, which exhibited suppressed neutrophil activity on day 2, showed minimal neutrophil presence on day 7 as well. Consequently, the numbers of Ly6G + pixels in suture and AgNPr-LASE groups were comparable to intact skin, but those in Cu-LASE group were significantly higher than the closure methods and in intact skin (Fig. 8b).

Similar to findings on day 2, the number of CD86⁺ pixels representing M1 macrophages were comparable among all groups on day 7 (Fig. 8c). M2 macrophages (Arg-1+ pixels) were elevated in suture and

Day 2 db/db mice

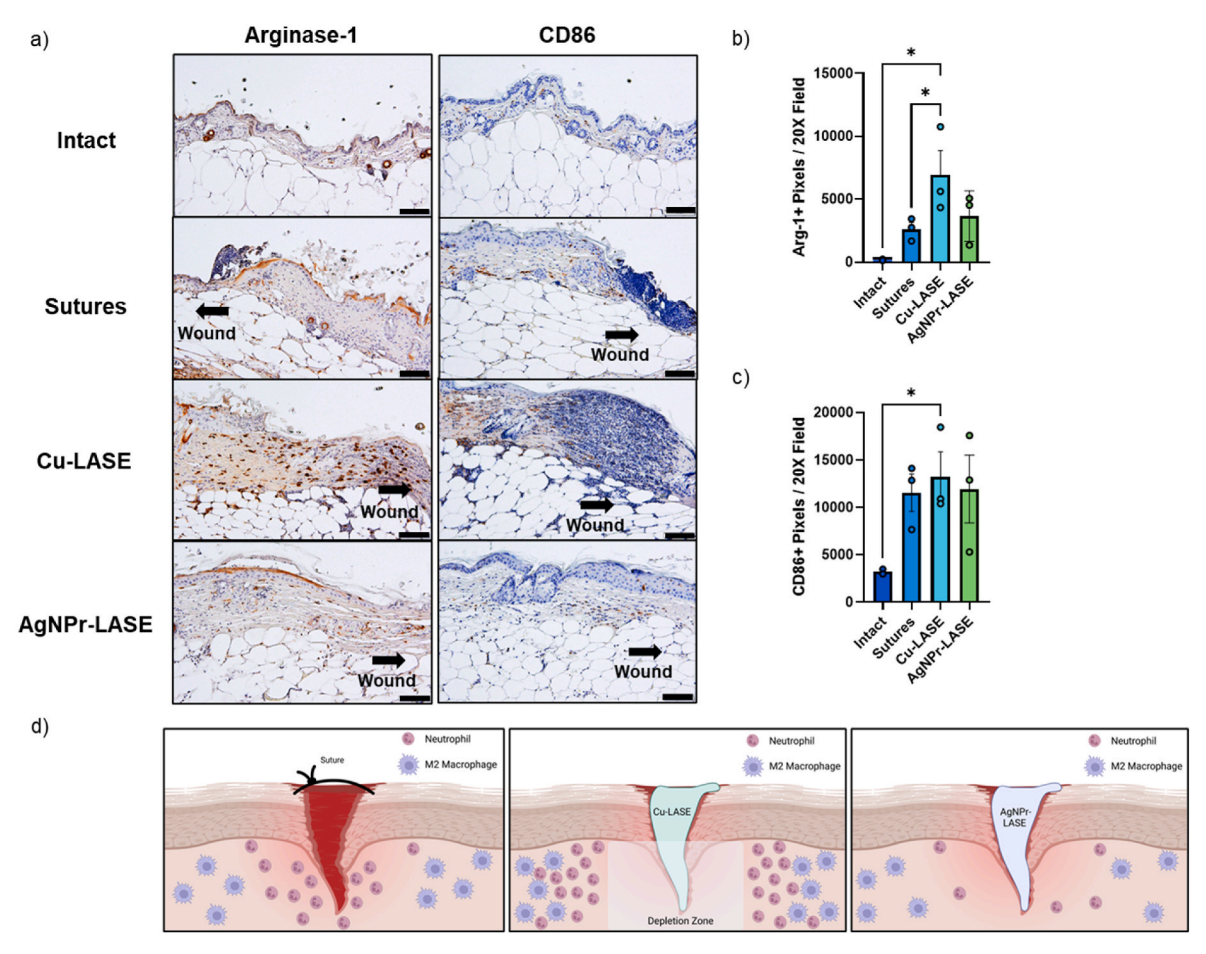


Fig. 7. Macrophage polarization and infiltration and neutrophil recruitment in the wound bed in db/db mice a) Representative microscopy images of incised skin closed with Cu-LASE, AgNPr-LASE, or sutures and intact skin; CD86⁺ ('M1') and Arginase-1+ ('M2') macrophages are stained brown in color. Scale bar: 100 µm. **b)** Number of Arginase-1+ and **c)** CD86⁺ pixels at the wound periphery **d)** Schematic of the effect of Cu-LASE, AgNPr-LASE, and sutures on innate immune cells in an incisional wound. One-way ANOVA followed by Fisher's LSD was used to identify statistically significant different groups in panels. *p < 0.05. (For interpretation of the references to color in this figure legend, the reader is referred to the Web version of this article.)

AgNPr-LASE groups compared to Cu-LASE (Fig. 8d). This indicates that Cu-LASE sealing results in higher numbers of M2 macrophages on day 2 than other groups but their levels deplete, falling below the levels of suture and AgNPr-LASE-closed wounds by day 7, likely as a result of copper toxicity. Arginase activity in keratinocytes is also important for their proliferation, migration, and differentiation [77]. Increased levels of arginase in the epidermal tongue are associated with increased rate of reepithelialization and closure [77]. Even though suture-closed wounds were completely reepithelialized, Arg-1 levels were found to be significantly lower in their epidermis, likely because the healing process had proceeded further towards completion. Among LASE groups, AgNPr-LASE showed significantly higher Arg-1 expression in the epidermal tongue compared to Cu-LASE, which validates a more pro-resolution nature of AgNPr-LASE compared to Cu-LASE.

Although copper is known to promote angiogenesis [54,78,79], the number of capillaries and myofibroblasts as determined from CD31 (endothelial marker) and α -smooth muscle actin (α -SMA; typically, a marker for myofibroblast differentiation) staining, respectively, were similar across the different groups on day 2 post closure. (Fig. S4, Supporting Information section). It is reported that neo-angiogenesis and fibroblast-to-myofibroblast differentiation are activated after day 2 post wounding [80,81]. Our results indicate that sutures or LASEs did not significantly influence angiogenesis and myofibroblast differentiation.

In later stages of wound repair, myofibroblast differentiation

typically occurs after the resolution of inflammatory phase and facilitates re-epithelialization, granulation, and angiogenesis [82]. Myofibroblast differentiation and activation are also associated in determining the quality of tissue repair given the involvement of these cells in collagen deposition and scarring [83]. Increased myofibroblast activity accelerates wound contraction, which facilitates quicker closure but is accompanied by increasing collagen deposition and scarring [84]. Consequently, different strategies are investigated to reduce myofibroblast activation [84]. We also observed a swarm of myofibroblasts at the site of reepithelialization in incisions closed with sutures (Fig. 9a). In addition, we observed higher numbers of α -SMA + pixels in incisions closed with sutures compared to those closed with LASE in db/db mice (Fig. 9b). It is likely that the tension caused by suture knots in the skin tissue create an environment with high and heterogenous mechanical stress that promotes scarring [51,85]. Therefore, the possibility and extent of scarring in suture-closed incisions is higher than shown in Fig. 9b compared to LASE-closed incisions.

Interestingly, we also observed increased endothelization in LASE-sealed incisions compared to those closed with sutures (Fig. 9c). As mentioned previously, copper is known to promote angiogenesis and increased endothelization in case of Cu-LASE is along expected lines. One explanation for the increased angiogenesis in LASEs, including in AgNPr-LASE, can be the activation of pro-reparative heat shock proteins that are upregulated in response to the laser-induced photothermal

Day 7 db/db mice

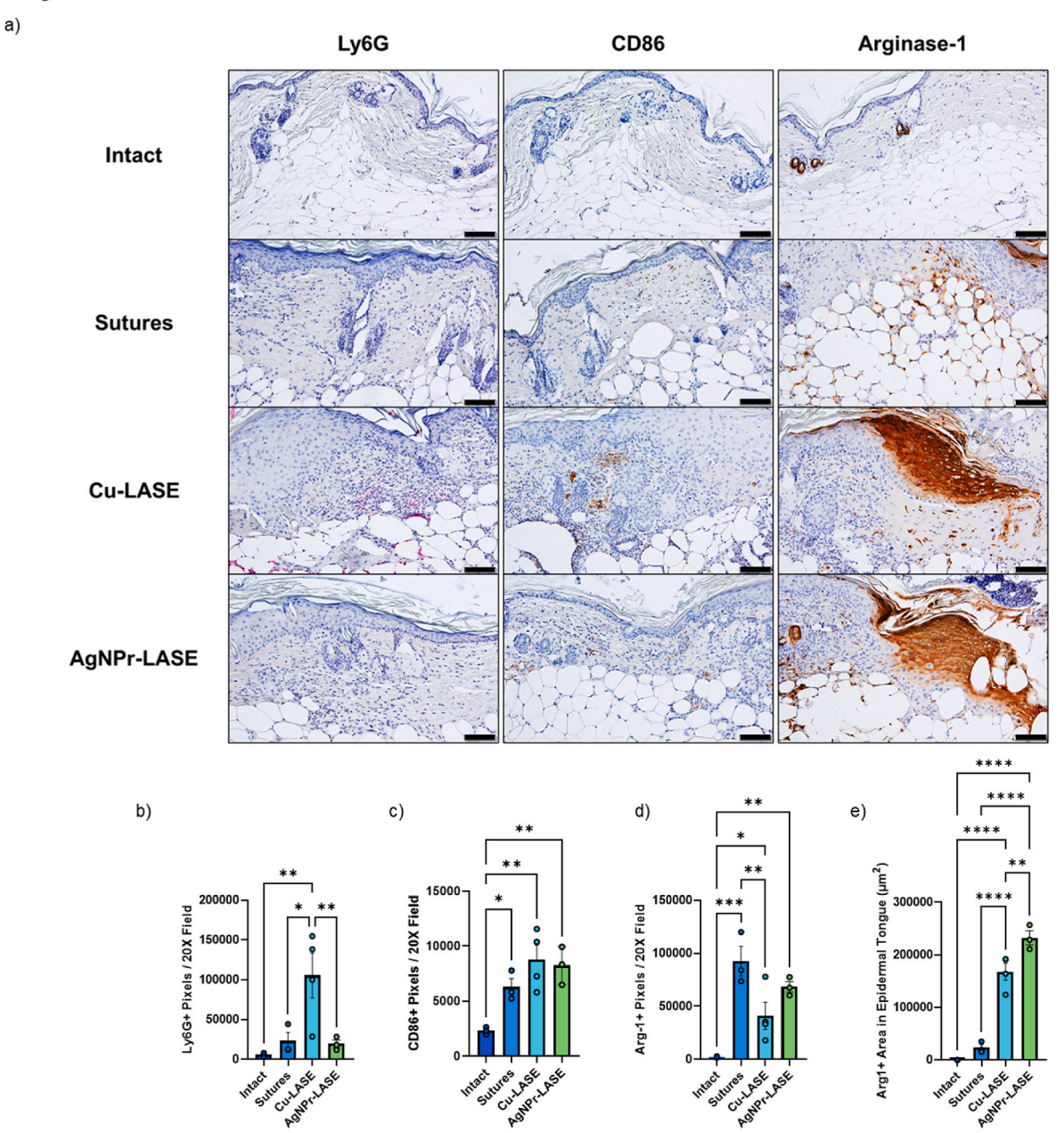


Fig. 8. Neutrophil activation and macrophage polarization in the incisional wound bed following LASE sealing or suturing in db/db mice 7 days post closure a) Skin sections stained for Ly6G (neutrophils in red), CD86 ('M1' macrophages in brown), and Arg-1 ('M2' macrophages in brown). Scale bar: $100 \mu m$ b, c, d) Quantitation of number of Ly6G+, CD86⁺, and Arg-1+ pixels in db/db mice 7 days post-closure. e) Arg-1+ area in the epidermal tongue. One-way ANOVA followed by Fisher's LSD was used to identify statistically significant differences in groups in panels. *p < 0.05; **p < 0.01; ***p < 0.001; ****p < 0.0001. (For interpretation of the references to color in this figure legend, the reader is referred to the Web version of this article.)

response [86–88] and future work will investigate their role in determining the efficacy of LASE-mediated tissue sealing and repair. It is noteworthy that endothelial cells lining the blood vessels also express $\alpha\textsc{-SMA}$ [89]. Considering higher endothelization observed in LASE groups with CD31 staining, it is likely that a portion of $\alpha\textsc{-SMA}$ signal can be attributed to the growing microvasculature network, which can imply that the signal specific to myofibroblasts is lower than shown in Fig. 9b.

3.6. Investigation of Antibacterial LASEs in vitro

Considering the efficacy and quality of repair associated with AgNPr-

LASE for biomechanical and barrier function recovery in diabetic and obese (db/db) mice (Figs. 3 and 4) and the significant clinical challenges associated with surgical site infections in diabetic patients, we investigated AgNPr-Vanc-LASEs in which the antibiotic drug, vancomycin, was incorporated into the AgNPr-LASE films for local delivery at the wound site. AgNPr-Vanc-LASEs were irradiated with a laser (65 °C, 2 min) to mimic *in vivo* sealing conditions, and release of vancomycin from these LASEs in PBS was determined using HPLC-based detection of the antibiotic. Initial loading of vancomycin in the LASE film was determined to be 30 \pm 3 $\mu g/mg$ film (from four films). Drug release profile revealed that $\sim\!40$ % of vancomycin was released within 15 min and $>\!90$ % of the drug was released within 2 h after incubation in PBS (Fig. 10a).

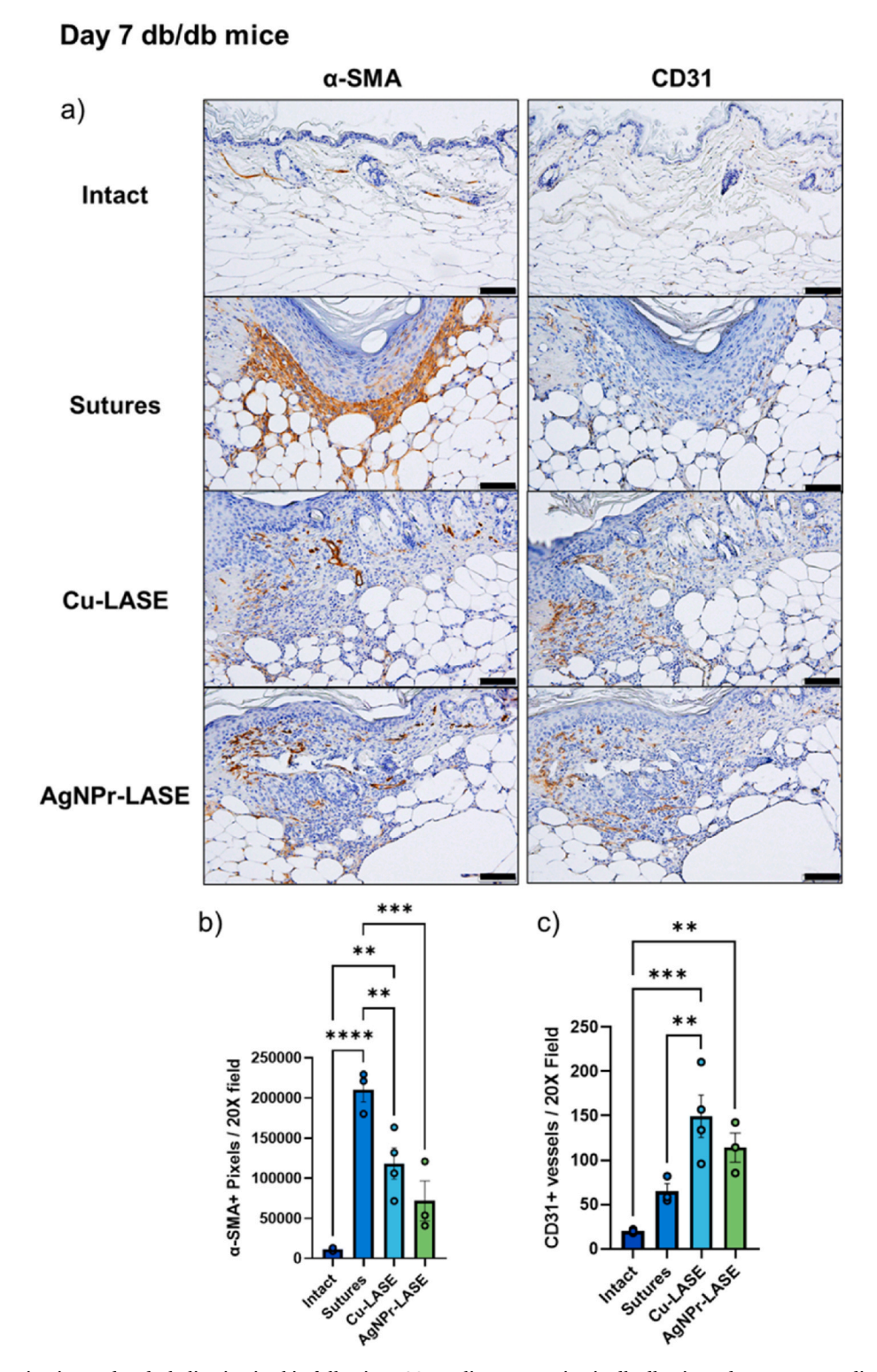


Fig. 9. Myofibroblast activation and endothelization in skin following LASE sealing or suturing in db/db mice 7 days post wounding. a) Serial skin sections stained for α-SMA (myofibroblasts in brown) and CD31 (blood vessels in brown). Scale bar: $100 \, \mu m$. b, c) Quantitation of number of α-SMA+ and CD31⁺ pixels in db/db mice 7 days post-surgery. One-way ANOVA followed by Fisher's LSD was used to identify the statistically significant differences in groups in panels. *p < 0.05; **p < 0.01; ***p < 0.001; ****p < 0.001; ****p < 0.0001. (For interpretation of the references to color in this figure legend, the reader is referred to the Web version of this article.)

However, the release profile of vancomycin from LASEs in a solution is likely significantly different from release in skin, where slower release may be expected because of the differential moisture content.

In vitro anti-MRSA activity of AgNPr-Vanc-LASE films was investigated using an agar assay and its performance was compared against antibacterial SECUROSORB $^{\text{TM}}$ PLUS sutures and AgNPr-LASE films

(without vancomycin). In this approach, a 1 cm incision was made in the agar, and the LASE or suture was inserted into this agar incision to mimic surgeries in mice. The agar incision was then inoculated with MRSA in a circle around the incision and tracked over time for 7 days. On day 1, we observed that AgNPr-Vanc-LASE inhibited MRSA growth with an efficacy comparable to that seen with SECUROSORBTM PLUS

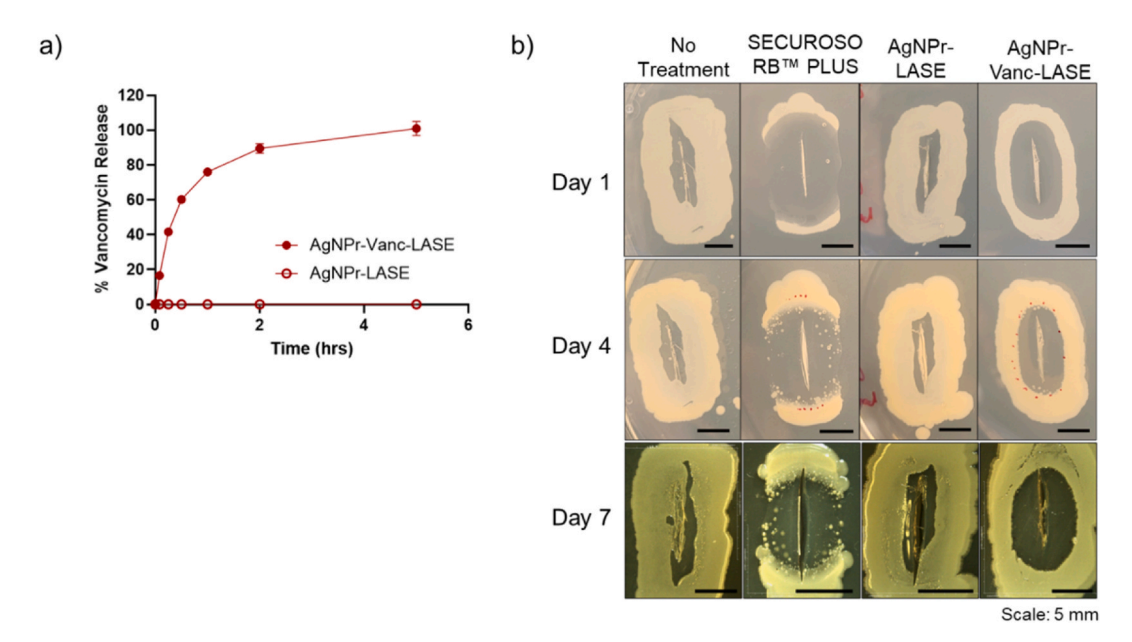


Fig. 10. Vancomycin release from AgNPr-Vanc-LASE and anti-MRSA activity of AgNPr-Vanc-LASE compared to SECUROSORB™ PLUS and AgNPr-LASE in vitro. a) Percent vancomycin released from AgNPr-Vanc-LASE in PBS determined using HPLC. b) Representative digital photographs (3 independently prepared films from one original silk batch) of agar plates containing a 1 cm incision either empty (no biomaterial) or containing different closure biomaterials – SECUROSORB™ PLUS antibacterial sutures, AgNPr-LASE, or AgNPr-Vanc-LASE – embedded in the agar incision and inoculated with MRSA in a circle around the incision. Photographs were taken on days 1, 4, and 7 post MRSA inoculation.

sutures (Fig. 10b). The chlorhexidine diacetate antimicrobial coating the SECUROSORB™ PLUS sutures is smaller and therefore diffused further into the agar than the larger vancomycin compound within AgNPr-Vanc-LASE, leading to a larger area of MRSA inhibition surrounding the SECUROSORB™ PLUS sutures (Fig. 10b). In contrast, AgNPr-LASE (without vancomycin) did not inhibit MRSA growth (Fig. 10b). Upon incubation for 7 days, AgNPr-Vanc-LASE continued inhibiting MRSA, while SECUROSORB™ PLUS sutures displayed decreased efficacy against MRSA over time (Fig. 10b). When the agar incision was directly inoculated with MRSA, SECUROSORB™ PLUS completely inhibited MRSA growth, likely due to rapid, direct contact killing (Fig. S5, Supporting Information section). AgNPr-Vanc-LASE initially inhibited MRSA, although MRSA cells located distal to the agar incision grew over a period of 7 days (Fig. S5, Supporting Information section).

3.7. Evaluation of anti-MRSA activity of AgNPr-Vanc-LASEs for Combating Surgical Site Infections in Diabetic and Obese Mice

A challenge model in which closed wounds in mice were inoculated with MRSA USA300, a clinically relevant MRSA strain, was used in these studies. MRSA bacterial loads in mouse skin were determined on day 0 (1 h post MRSA inoculation) as well as at 7 days post closure and MRSA challenge. The digital photographs of the incisions are shown in Fig. 11a. In these studies, db/db mice in which vancomycin (5 mg/kg in $20~\mu L$) was administered directly to the wound and closed with nylon sutures (Nylon-Vanc) demonstrated the lowest MRSA levels on day 7 (Fig. 11b), likely because of the immediate local availability of the antibiotic in high concentrations. Nylon sutures and the AgNPr-LASE (without vancomycin) were ineffective at combating the MRSA infection; the bacterial burden increased ~2 log₁₀ CFU after 7 days, compared to initial MRSA inoculation levels on day 0 (Fig. 11a and b). AgNPr-LASE films without vancomycin were not effective in combating infection despite the presence of silver nanoprisms, likely because of unavailability of sufficient amounts of free silver ions, which are considered responsible for antibacterial activity [87].

AgNPr-Vanc-LASEs significantly reduced MRSA bacterial load in db/db mice by an average $\sim 2 \log_{10}$ CFU compared to the initial inoculation levels (p=0.006) and were as effective as the commercial antibacterial,

absorbable SECUROSORBTM PLUS sutures (Fig. 11b). Compared to AgNPr-LASEs, vancomycin-loaded AgNPr-Vanc-LASEs demonstrated improved macroscopic appearance of MRSA-infected closed incisions (Fig. 11a) and significantly decreased MRSA tissue burden $\sim\!4\log_{10}(p<0.0001;$ Fig. 11b). Thus, a significant benefit was observed when vancomycin was incorporated within AgNPr-LASE films, compared to LASE films without the drug. It is possible to increase drug loading in LASEs and/or improve drug release properties from silk to further enhance efficacy of AgNPr-Vanc-LASEs. Overall, these results indicate that AgNPr-LASEs not only demonstrate sealing activity in diabetic and obese mice but can also be used to load and deliver antibacterial drugs for combating surgical site infections, which are a clinical challenge in diabetic and obese individuals.

Histological evaluation of the MRSA-challenged skin followed by different approximation and SSI-combating methods provided significant insights into wound/skin health. Incisions closed with AgNPr-LASE, SECUROSORB™ PLUS, and nylon sutures showed a large number of cells present within and around the wounds on day 7 post treatment as indicated by red circles in Fig. 12a. The wounds in these groups were also characterized by presence of a thick scab over the incision and evidence of edema as indicated by the region in these red circles in Fig. 12a. Conversely, wounds treated with vancomycin − either added directly into the wound followed by closure with nylon sutures (Nylon-Vanc) or embedded in the LASE (AgNPr-Vanc-LASE) − did not exhibit such signs of severe inflammation (Fig. 12a). As before, AgNPr-LASE demonstrated a statistically significant epidermal gap compared to nylon sutures or nylon sutures + vancomycin (Nylon-Vanc), but the gap with AgNPr-Vanc-LASE was not statistically significant (Fig. 12b).

Histological sections of MRSA-challenged wounds were also semiquantitatively evaluated by two experts blinded to sample information. A visual analog scale (VAS) was adapted from Nussbaum et al. [90] and is shown in Table S1 (Supporting Information section). Considering two wound healing stages relevant to the current study and timeframe, each histological section was assigned an inflammation score and a remodeling score (Fig. 12c). The inflammation score was obtained by adding edema, leucocytes, and macrophages scores, while the remodeling score was obtained by adding granulation tissue, fibroblasts, collagen, and epithelialization scores (Table S1) [90]. The average

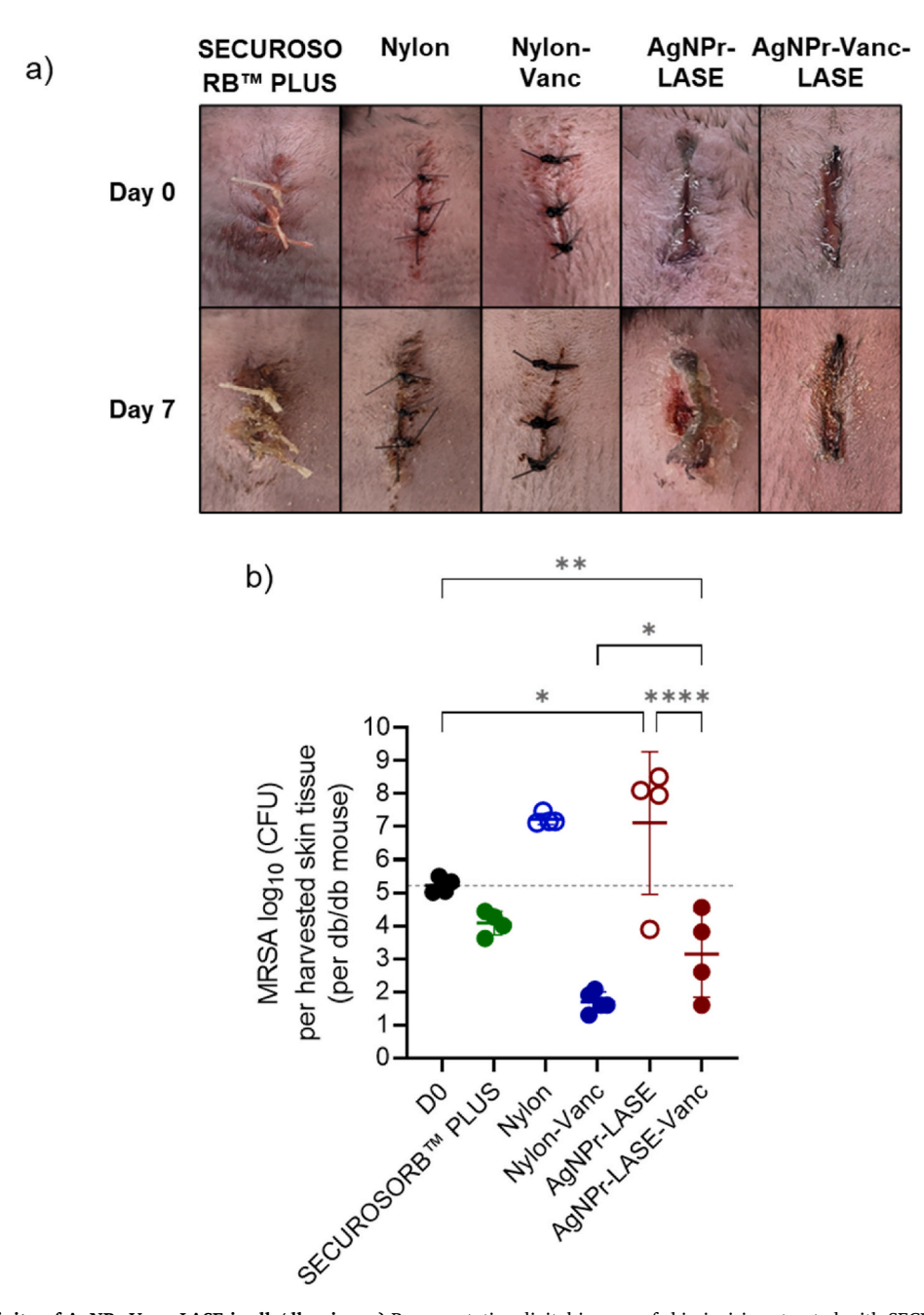


Fig. 11. Anti-MRSA activity of AgNPr-Vanc-LASE in db/db mice. a) Representative digital images of skin incisions treated with SECUROSORBTM PLUS sutures, nylon, nylon-Vanc, AgNPr-LASE, and AgNPr-Vanc-LASE. b) MRSA load quantitation per harvested skin tissue in different groups (n = 4 per group) of db/db mice. Data include the mean and SD. The hatched line indicates the average day 0 (D0) MRSA load. *, p < 0.05; **p < 0.01; ****p < 0.001; one-way ANOVA.

inflammation score of AgNPr-Vanc-LASE was significantly lower than that of the SECUROSORB™ PLUS, AgNPr-LASE, and Nylon groups and comparable to the Nylon-Vanc group (Fig. 12c). These Nylon-Vanc and AgNPr-Vanc-LASE results are consistent with the antibacterial action of vancomycin, which significantly reduced the MRSA load (Fig. 11b), thereby reducing local inflammation at the surgical site. The remodeling score of AgNPr-Vanc-LASE was comparable with all other treatments (Fig. 12c), indicating little difference in fibroblast activity and collagen deposition between the treatment groups. Taken together, AgNPr-Vanc-LASE demonstrated effective anti-MRSA activity in a challenge model, which mimics surgical site infections, and the efficacy of this approach can be enhanced by loading higher amounts of the antibacterial drug. Vancomycin-loaded LASEs also resulted in lower inflammation of the MRSA-infected tissue than other approximation approaches, which demonstrates the overall utility of this approach

especially in diabetic hosts, who are prone to surgical site infections.

4. Conclusions

Limitations including wound dehiscence, inflammation, scarring, and risk of infection reduce the efficacy of conventional approximation devices, such as sutures, particularly in diabetic and obese individuals. Our current study demonstrated that laser-activated sealants, especially AgNPr-LASE, are effectively able to seal incisional wounds in four different strains of mice, including in diabetic and obese (db/db) mice. The choice of photothermal converter in LASE significantly affected wound closure and tissue repair outcomes. Copper chloride-loaded LASE caused local inflammation and toxicity, but there may yet be use for copper in local infection control and angiogenesis at concentrations lower than those needed for effective photothermal response and

Day 7 db/db mice MRSA Infection

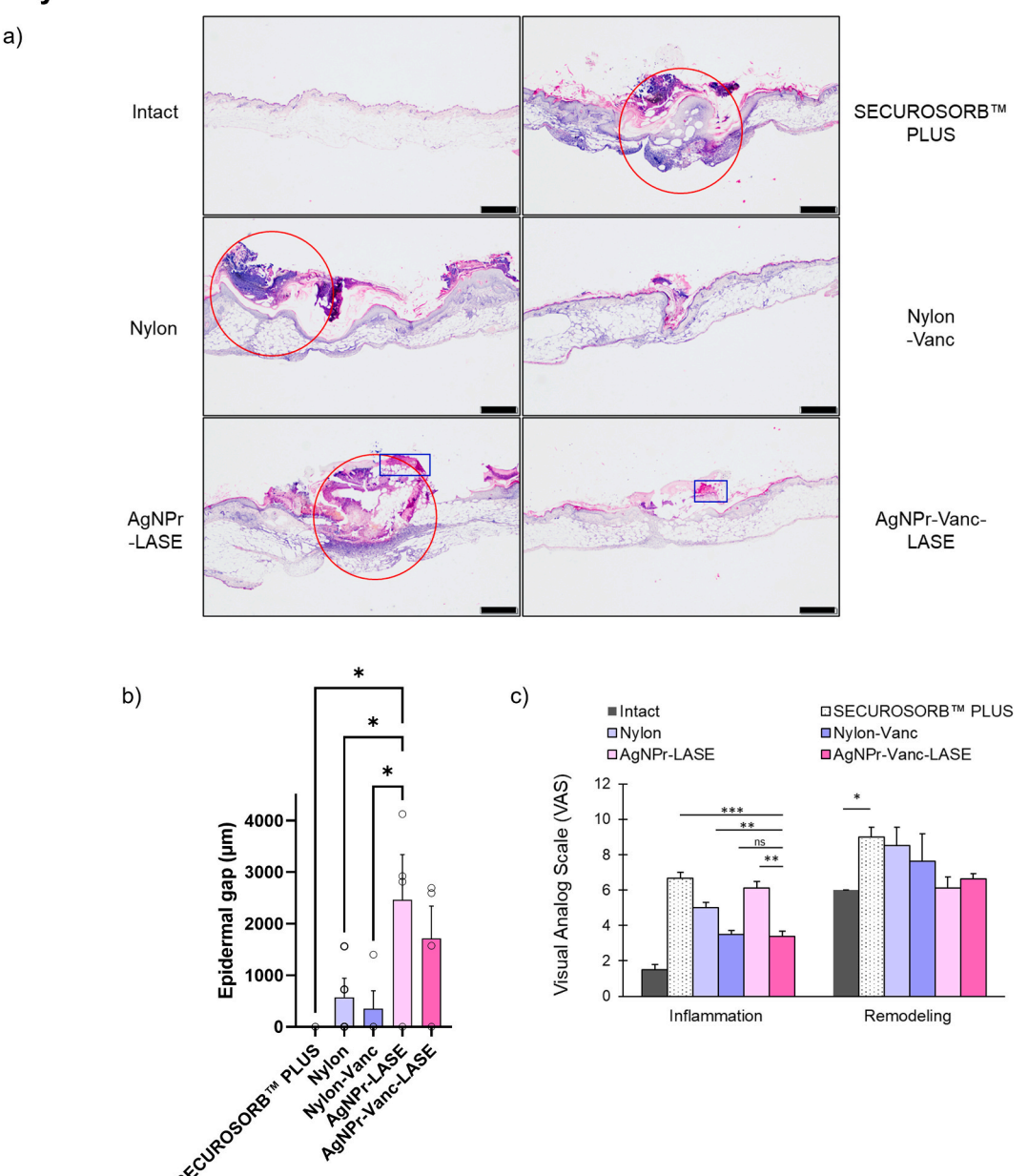


Fig. 12. Hematoxylin and eosin staining of MRSA-challenged incisions with different treatments in db/db mice. a) Representative histological images of wounds. Red circles indicate regions of high cell infiltration and edema. Blue squares indicate dermal collagen denaturation in LASE-treated wounds. Scale bar = 500 μ m. b) Quantification of epidermal gap in all treatments (n = 4 for all groups except n = 3 for SECUROSORBTM PLUS. c) Visual Analog Scale (VAS) scores of the histological sections (average of two blinded expert evaluators). *, p < 0.05; **p < 0.05; **p < 0.01; one-way ANOVA followed by Fisher's LSD. (For interpretation of the references to color in this figure legend, the reader is referred to the Web version of this article.)

sealing. Conversely, use of silver nanoprism-embedded LASE (AgNPr-LASE) resulted in lower inflammation, higher biomechanical recoveries, increased angiogenesis, and lower myofibroblast activation when compared to nylon sutures; higher myofibroblast activation likely indicated propensity for higher scarring in case of sutures when compared to AgNPr-LASE. However, nylon sutures performed better than LASEs in restoring epidermal structure and function, likely because of presence of the LASE biomaterial between the epidermal edges at the wound site. In addition, AgNPr-LASEs also demonstrated multifunctionality as depots for local antibiotic (vancomycin) delivery as an approach for prophylactic control of MRSA infections in diabetic and obese mice. In addition to effectively combating MRSA infections in a challenge model, AgNPr-Vanc-LASE also resulted in minimal

inflammation at the wound site, likely as a result of vancomycin-mediated bacterial control. Thus, the LASE approach represents a balance between kinetics of closure and quality of tissue repair in diabetic, obese mice. Lasers are used widely in dermatologic applications, and it may be possible for the LASE technology to be eventually adopted. Although hand-held NIR lasers are an additional requirement for this technology, they likely do not represent a huge infrastructure investment. The potential for thermal damage with the LASE approach will need appropriate training for their safe application for successful translation. Taken together, AgNPr-LASE sealing is a promising approach that facilitates skin closure while resulting in improved quality of repair compared to sutures and can be used as multifunctional bioactive devices in individuals with underlying pathologies that elevate

risks of adverse wound healing outcomes, including infection and scarring.

Conflict of interest disclosure

KR is affiliated with Synergyan, LLC and Endotat Biotechnologies, LLC. JRY is affiliated with Endotat Biotechnologies, LLC and Vivo Bioconsulting, LLC.

CRediT authorship contribution statement

Shubham Pallod: Conceptualization, Data curation, Formal analysis, Investigation, Methodology, Software, Visualization, Writing original draft, Writing - review & editing. Rodrigo Aguilera Olvera: Data curation, Formal analysis, Investigation, Methodology, Validation, Visualization, Writing - original draft. Deepanjan Ghosh: Investigation, Methodology. Lama Rai: Investigation. Souzan Brimo: Investigation. Weston DeCambra: Data curation. Formal analysis. Investigation, Methodology, Writing – original draft. Harsh Girish Sant: Formal analysis, Investigation. Eron Ristich: Formal analysis, Methodology. Vanshika Singh: Investigation. Muhammad Raisul Abedin: Investigation. Nicolas Chang: Investigation. Jeffery L. Yarger: Conceptualization, Formal analysis, Methodology, Writing review & editing. Jung Keun Lee: Formal analysis, Validation. Jacquelyn Kilbourne: Investigation, Methodology, Supervision. Jordan R. Yaron: Methodology, Validation, Writing - review & editing. Shelley E. Haydel: Conceptualization, Methodology, Supervision, Writing - original draft, Writing - review & editing. Kaushal Rege: Conceptualization, Funding acquisition, Project administration, Resources, Supervision, Validation, Writing - original draft, Writing - review & editing.

Declaration of competing interest

The authors declare the following financial interests/personal relationships which may be considered as potential competing interests: Kaushal Rege reports financial support was provided by National Institutes of Health. Jordan R. Yaron reports financial support was provided by National Institutes of Health. Jeffery L. Yarger reports financial support was provided by National Science Foundation. Kaushal Rege reports a relationship with Endotat Biotechnologies, LLC that includes: board membership. Jordan R. Yaron reports a relationship with Endotat Biotechnologies, LLC that includes: board membership. Kaushal Rege has patent issued to Arizona Board of Regents on Behalf of Arizona State University. If there are other authors, they declare that they have no known competing financial interests or personal relationships that could have appeared to influence the work reported in this paper.

Data availability

Data will be made available on request.

Acknowledgments

The authors are grateful to the National Institutes of Health (R21 AI147279 to KR) for funding this research. JRY would like to acknowledge K01 EB031984 for partial support. KR would also like to acknowledge R01 AR074627 for partial support of this research. JLY and KR would like to acknowledge the National Science Foundation (DMR 2105312) for partial support of this work. The authors thank Inam Ridha for helpful discussions on silver nanoprisms and Dr. Sudhakar Godeshala, Assistant Research Scientist in CBIT, Biodesign Institute, ASU, for help with copper release studies from LASE films.

Appendix A. Supplementary data

Supplementary data to this article can be found online at https://doi.org/10.1016/j.biomaterials.2024.122668.

References

- [1] G.C. Gurtner, S. Werner, Y. Barrandon, M.T. Longaker, Wound repair and regeneration, Nature 453 (7193) (2008) 314–321, https://doi.org/10.1038/nature/07030
- [2] S.A. Eming, P. Martin, M. Tomic-Canic, Wound repair and regeneration: mechanisms, signaling, and translation, Sci. Transl. Med. 6 (265) (2014) 265sr6, https://doi.org/10.1126/scitranslmed.3009337.
- [3] R.E. Mirza, M.M. Fang, E.M. Weinheimer-Haus, W.J. Ennis, T.J. Koh, Sustained inflammasome activity in macrophages impairs wound healing in type 2 diabetic humans and mice, Diabetes 63 (3) (2014) 1103–1114, https://doi.org/10.2337/ db13.0027
- [4] T. Bouchery, N. Harris, Neutrophil-macrophage cooperation and its impact on tissue repair, Immunol. Cell Biol. 97 (3) (2019) 289–298, https://doi.org/10.1111/ imch 12241
- [5] N. Strbo, N. Yin, O. Stojadinovic, Innate and adaptive immune responses in wound epithelialization, Adv. Wound Care 3 (7) (2014) 492–501, https://doi.org/ 10.1089/wound.2012.0435.
- [6] S. Guo, L.A. Dipietro, Factors affecting wound healing, J. Dent. Res. 89 (3) (2010) 219–229, https://doi.org/10.1177/0022034509359125.
- [7] S.S. Mathew-Steiner, S. Roy, C.K. Sen, Collagen in wound healing, Bioengineering 8 (5) (2021), https://doi.org/10.3390/bioengineering8050063.
- [8] G. Danaei, M.M. Finucane, Y. Lu, G.M. Singh, M.J. Cowan, C.J. Paciorek, J.K. Lin, F. Farzadfar, Y.H. Khang, G.A. Stevens, M. Rao, M.K. Ali, L.M. Riley, C.A. Robinson, M. Ezzati, G. Global, Burden of Metabolic Risk Factors of Chronic Diseases Collaborating, National, regional, and global trends in fasting plasma glucose and diabetes prevalence since 1980: systematic analysis of health examination surveys and epidemiological studies with 370 country-years and 2.7 million participants, Lancet 378 (9785) (2011) 31–40, https://doi.org/10.1016/S0140-6736(11)60679-X.
- [9] J.L. Burgess, W.A. Wyant, B. Abdo Abujamra, R.S. Kirsner, I. Jozic, Diabetic wound-healing science, Medicina (Kaunas) 57 (10) (2021), https://doi.org/ 10.3390/medicina57101072.
- [10] D.G. Armstrong, M.A. Swerdlow, A.A. Armstrong, M.S. Conte, W.V. Padula, S. A. Bus, Five year mortality and direct costs of care for people with diabetic foot complications are comparable to cancer, J. Foot Ankle Res. 13 (1) (2020) 16, https://doi.org/10.1186/s13047-020-00383-2.
- [11] S. Tsalamandris, A.S. Antonopoulos, E. Oikonomou, G.A. Papamikroulis, G. Vogiatzi, S. Papaioannou, S. Deftereos, D. Tousoulis, The role of inflammation in diabetes: current concepts and future perspectives, Eur. Cardiol. 14 (1) (2019) 50–59, https://doi.org/10.15420/ecr.2018.33.1.
- [12] R. Ogawa, Keloid and hypertrophic scars are the result of chronic inflammation in the reticular dermis, Int. J. Mol. Sci. 18 (3) (2017), https://doi.org/10.3390/ ijms18030606.
- [13] C. Huang, R. Ogawa, Role of inflammasomes in keloids and hypertrophic scarslessons learned from chronic diabetic wounds and skin fibrosis, Int. J. Mol. Sci. 23 (12) (2022), https://doi.org/10.3390/ijms23126820.
- [14] E.T. Martin, K.S. Kaye, C. Knott, H. Nguyen, M. Santarossa, R. Evans, E. Bertran, L. Jaber, Diabetes and risk of surgical site infection: a systematic review and metaanalysis, Infect. Control Hosp. Epidemiol. 37 (1) (2016) 88–99, https://doi.org/ 10.1017/ice.2015.249
- [15] N. Dasari, A. Jiang, A. Skochdopole, J. Chung, E.M. Reece, J. Vorstenbosch, S. Winocour, Updates in diabetic wound healing, inflammation, and scarring, Semin. Plast. Surg. 35 (3) (2021) 153–158, https://doi.org/10.1055/s-0041-1731460
- [16] J. Sanchez, F. Antonicelli, D. Tuton, S. Mazouz Dorval, C. Francois, [Specificities in children wound healing], Ann. Chir. Plast. Esthet. 61 (5) (2016) 341–347, https://doi.org/10.1016/j.anplas.2016.05.001.
- [17] A.M. Tatara, D.P. Kontoyiannis, A.G. Mikos, Drug delivery and tissue engineering to promote wound healing in the immunocompromised host: current challenges and future directions, Adv. Drug Deliv. Rev. 129 (2018) 319–329, https://doi.org/ 10.1016/j.addr.2017.12.001.
- [18] F. Coccolini, M. Improta, E. Cicuttin, F. Catena, M. Sartelli, R. Bova, N. De' Angelis, S. Gitto, D. Tartaglia, C. Cremonini, C. Ordonez, G.L. Baiocchi, M. Chiarugi, Surgical site infection prevention and management in immunocompromised patients: a systematic review of the literature, World J. Emerg. Surg. 16 (1) (2021) 33, https://doi.org/10.1186/s13017-021-00375-y.
- [19] J.L. Seidelman, C.R. Mantyh, D.J. Anderson, Surgical site infection prevention: a review, JAMA 329 (3) (2023) 244–252, https://doi.org/10.1001/ iama 2022 24075
- [20] B. Tserenpuntsag, V. Haley, P. Ann Hazamy, A. Eramo, R. Knab, M. Tsivitis, E. J. Clement, Risk factors for surgical site infection after abdominal hysterectomy, New York State, 2015-2018, Am. J. Infect. Control 51 (5) (2023) 539–543, https://doi.org/10.1016/j.ajic.2023.01.016.
- [21] M.A. Olsen, J.J. Nepple, K.D. Riew, L.G. Lenke, K.H. Bridwell, J. Mayfield, V. J. Fraser, Risk factors for surgical site infection following orthopaedic spinal operations, J Bone Joint Surg Am 90 (1) (2008) 62–69, https://doi.org/10.2106/JBJS.F.01515.

- [22] S. Chen, M.V. Anderson, W.K. Cheng, M.D. Wongworawat, Diabetes associated with increased surgical site infections in spinal arthrodesis, Clin. Orthop. Relat. Res. 467 (7) (2009) 1670–1673, https://doi.org/10.1007/s11999-009-0740-y.
- [23] D.K. Wukich, B.E. Crim, R.G. Frykberg, B.L. Rosario, Neuropathy and poorly controlled diabetes increase the rate of surgical site infection after foot and ankle surgery, J Bone Joint Surg Am 96 (10) (2014) 832–839, https://doi.org/10.2106/ ibis.L.01302.
- [24] M.S. Reich, I. Fernandez, A. Mishra, L. Kafchinski, A. Adler, M.P. Nguyen, Diabetic control predicts surgical site infection risk in orthopaedic trauma patients, J. Orthop. Trauma 33 (10) (2019) 514–517, https://doi.org/10.1097/ bot.0000000000001512.
- [25] J. Lai, Q. Li, Y. He, S. Zou, X. Bai, S. Rastogi, Glycemic control regimens in the prevention of surgical site infections: a meta-analysis of randomized clinical trials, Frontiers in Surgery (2022) 9, https://doi.org/10.3389/fsurg.2022.855409.
- [26] A. Ata, J. Lee, S.L. Bestle, J. Desemone, S.C. Stain, Postoperative hyperglycemia and surgical site infection in general surgery patients, Arch. Surg. 145 (9) (2010) 858–864, https://doi.org/10.1001/archsurg.2010.179.
- [27] E.M. Zardi, N. Montelione, R.C. Vigliotti, C. Chello, D.M. Zardi, F. Spinelli, F. Stilo, Surgical wound dehiscence complicated by methicillin-resistant Staphylococcus aureus infection in a diabetic patient with femorotibial vascular bypass occlusion, Clin. Med. 20 (1) (2020) 98–100, https://doi.org/10.7861/clinmed.2019-0392.
- [28] M. Zubair, J. Ahmad, Potential risk factors and outcomes of infection with multidrug resistance among diabetic patients having ulcers: 7 years study, Diabetes Metab Syndr 13 (1) (2019) 414–418, https://doi.org/10.1016/j.dsx.2018.10.014.
- [29] J.A. Suaya, D.F. Eisenberg, C. Fang, L.G. Miller, Skin and soft tissue infections and associated complications among commercially insured patients aged 0-64 years with and without diabetes in the U.S, PLoS One 8 (4) (2013) e60057, https://doi. org/10.1371/journal.pone.0060057.
- [30] H.J. Stacey, C.S. Clements, S.C. Welburn, J.D. Jones, The prevalence of methicillinresistant Staphylococcus aureus among diabetic patients: a meta-analysis, Acta Diabetol. 56 (8) (2019) 907–921, https://doi.org/10.1007/s00592-019-01301-0.
- [31] B.A. Lipsky, Y.P. Tabak, R.S. Johannes, L. Vo, L. Hyde, J.A. Weigelt, Skin and soft tissue infections in hospitalised patients with diabetes: culture isolates and risk factors associated with mortality, length of stay and cost, Diabetologia 53 (5) (2010) 914–923, https://doi.org/10.1007/s00125-010-1672-5.
- [32] N.A. Turner, B.K. Sharma-Kuinkel, S.A. Maskarinec, E.M. Eichenberger, P.P. Shah, M. Carugati, T.L. Holland, V.G. Fowler Jr., Methicillin-resistant Staphylococcus aureus: an overview of basic and clinical research, Nat. Rev. Microbiol. 17 (4) (2019) 203–218, https://doi.org/10.1038/s41579-018-0147-4.
- [33] F.C. Tenover, R.V. Goering, Methicillin-resistant Staphylococcus aureus strain USA300: origin and epidemiology, J. Antimicrob. Chemother. 64 (3) (2009) 441–446. https://doi.org/10.1093/jac/dkp241.
- [34] Y. Huang, E.R. Cadet, M.W. King, J.H. Cole, Comparison of the mechanical properties and anchoring performance of polyvinylidene fluoride and polypropylene barbed sutures for tendon repair, J. Biomed. Mater. Res. B Appl. Biomater. 110 (10) (2022) 2258–2265. https://doi.org/10.1002/jbm.b.35074.
- [35] L. Xu, Y. Liu, W. Zhou, D. Yu, Electrospun medical sutures for wound healing: a review, Polymers 14 (9) (2022), https://doi.org/10.3390/polym14091637.
- [36] P.G. Gouletsou, N.N. Prassinos, L.G. Papazoglou, P. Kostoulas, A.D. Galatos, Comparison of continuous intradermal with simple interrupted suture pattern: an experimental study in dogs, Top. Companion Anim. Med. 41 (2020) 100454, https://doi.org/10.1016/j.tcam.2020.100454.
- [37] W. Luo, Y. Tao, Y. Wang, Z. Ouyang, J. Huang, X. Long, Comparing running vs interrupted sutures for skin closure: a systematic review and meta-analysis, Int. Wound J. 20 (1) (2023) 210–220, https://doi.org/10.1111/iwj.13863.
- [38] J. Schimmel, M. Belcher, C. Vieira, N. Lawrence, A. Decker, Incidence of surgical site infections in second intention healing after dermatologic surgery, Dermatol. Surg. 46 (12) (2020) 1492–1497, https://doi.org/10.1097/ DSS.0000000000002409.
- [39] E. Maurer, A. Reuss, K. Maschuw, B. Aminossadati, T. Neubert, C. Schade-Brittinger, D.K. Bartsch, Superficial surgical site infection following the use of intracutaneous sutures versus staples, Dtsch Arztebl Int 116 (21) (2019) 365–371, https://doi.org/10.3238/arztebl.2019.0365.
- [40] P.M. Costa, D.A. Learmonth, D.B. Gomes, M.P. Cautela, A.C.N. Oliveira, R. Andrade, J. Espregueira-Mendes, T.R. Veloso, C.B. Cunha, R.A. Sousa, Mussel-Inspired catechol functionalisation as a strategy to enhance biomaterial adhesion: a systematic review, Polymers 13 (19) (2021), https://doi.org/10.3390/ polymer/100217
- [41] S. Li, J. Zhou, Y. Huang, J. Roy, N. Zhou, K. Yum, X. Sun, L. Tang, Injectable click chemistry-based bioadhesives for accelerated wound closure, Acta Biomater. 110 (2020) 95–104, https://doi.org/10.1016/j.actbio.2020.04.004.
- [42] T.M. Lutz, C. Kimna, A. Casini, O. Lieleg, Bio-based and bio-inspired adhesives from animals and plants for biomedical applications, Mater Today Bio 13 (2022) 100203, https://doi.org/10.1016/j.mtbio.2022.100203.
- [43] S. Fluellen, K. Mackey, K. Hagglund, M.F. Aslam, Randomized clinical trial comparing skin closure with tissue adhesives vs subcuticular suture after robotic urogynecologic procedures, World J. Methodol. 10 (1) (2020) 1–6, https://doi.org/ 10.5662/wjm.v10.i1.1.
- [44] E. Lee, A. Elzomor, C. Zwemer, A. Chen, P.G. Thakkar, Complications associated with Dermabond(R) during head and neck surgery: MAUDE and literature review, Am. J. Otolaryngol. 43 (2) (2022) 103330, https://doi.org/10.1016/j. amjoto.2021.103330.
- [45] R. Urie, C. Guo, D. Ghosh, M. Thelakkaden, V. Wong, J.K. Lee, J. Kilbourne, J. Yarger, K. Rege, Rapid soft tissue approximation and repair using laser-activated silk nanosealants, Adv. Funct. Mater. 28 (42) (2018) 1802874, https://doi.org/ 10.1002/adfm.201802874.

[46] D. Simhon, M. Halpern, T. Brosh, T. Vasilyev, A. Ravid, T. Tennenbaum, Z. Nevo, A. Katzir, Immediate tight sealing of skin incisions using an innovative temperature-controlled laser soldering device: in vivo study in porcine skin, Ann. Surg. 245 (2) (2007) 206–213, https://doi.org/10.1097/01.

- [47] H.C. Huang, C.R. Walker, A. Nanda, K. Rege, Laser welding of ruptured intestinal tissue using plasmonic polypeptide nanocomposite solders, ACS Nano 7 (4) (2013) 2988–2998, https://doi.org/10.1021/nn303202k.
- [48] R. Urie, S. Quraishi, M. Jaffe, K. Rege, Gold nanorod-collagen nanocomposites as photothermal nanosolders for laser welding of ruptured porcine intestines, ACS Biomater. Sci. Eng. 1 (9) (2015) 805–815, https://doi.org/10.1021/ archiomaterials 5b00174
- [49] M. Mushaben, R. Urie, T. Flake, M. Jaffe, K. Rege, J. Heys, Spatiotemporal modeling of laser tissue soldering using photothermal nanocomposites, Laser Surg. Med. 50 (2) (2018) 143–152, https://doi.org/10.1002/lsm.22746.
- [50] R. Urie, M. McBride, D. Ghosh, A. Fattahi, R. Nitiyanandan, J. Popovich, J.J. Heys, J. Kilbourne, S.E. Haydel, K. Rege, Antimicrobial laser-activated sealants for combating surgical site infections, Biomater. Sci. 9 (10) (2021) 3791–3803, https://doi.org/10.1039/d0bm01438a.
- [51] I. Ridha, A. Basiri, S. Godeshala, M.Z.E. Rafique, D. Ghosh, J. Williams, N. Chawla, J.K. Lee, J. Kilbourne, Y. Yao, K. Rege, Chromophore-free sealing and repair of soft tissues using mid-infrared light-activated biosealants, Adv. Funct. Mater. 31 (6) (2021) 2007811, https://doi.org/10.1002/adfm.202007811.
- [52] D. Ghosh, S. Godeshala, R. Nitiyanandan, M.S. Islam, J.R. Yaron, D. DiCaudo, J. Kilbourne, K. Rege, Copper-eluting fibers for enhanced tissue sealing and repair, ACS Appl. Mater. Interfaces 12 (25) (2020) 27951–27960, https://doi.org/ 10.1021/acsami.0c04755.
- [53] P. Rajasekaran, S. Santra, Hydrothermally treated chitosan hydrogel loaded with copper and zinc particles as a potential micronutrient-based antimicrobial feed additive, Front. Vet. Sci. 2 (2015) 62, https://doi.org/10.3389/fvets.2015.00062.
- [54] C.K. Sen, S. Khanna, M. Venojarvi, P. Trikha, E.C. Ellison, T.K. Hunt, S. Roy, Copper-induced vascular endothelial growth factor expression and wound healing, Am. J. Physiol. Heart Circ. Physiol. 282 (5) (2002) H1821–H1827, https://doi.org/ 10.1152/ajpheart.01015.2001.
- [55] E. Takeda, W. Xu, M. Terakawa, T. Niidome, Tailored structure and antibacterial properties of silica-coated silver nanoplates by pulsed laser irradiation, ACS Omega 7 (8) (2022) 7251–7256, https://doi.org/10.1021/acsomega.1c07058.
- [56] C. Toparli, S.W. Hieke, A. Altin, O. Kasian, C. Scheu, A. Erbe, State of the surface of antibacterial copper in phosphate buffered saline, J. Electrochem. Soc. 164 (12) (2017) H734–H742, https://doi.org/10.1149/2.0351712jes.
- [57] G. He, W. Hu, C.M. Li, Spontaneous interfacial reaction between metallic copper and PBS to form cupric phosphate nanoflower and its enzyme hybrid with enhanced activity, Colloids Surf. B Biointerfaces 135 (2015) 613–618, https://doi. org/10.1016/j.colsurfb.2015.08.030.
- [58] P. Bogdanov, L. Corraliza, J.A. Villena, A.R. Carvalho, J. Garcia-Arumi, D. Ramos, J. Ruberte, R. Simo, C. Hernandez, The db/db mouse: a useful model for the study of diabetic retinal neurodegeneration, PLoS One 9 (5) (2014) e97302, https://doi.org/10.1371/journal.pone.0097302
- [59] P. Huynh, J. Phie, S.M. Krishna, J. Golledge, Systematic review and meta-analysis of mouse models of diabetes-associated ulcers, BMJ Open Diabetes Res Care 8 (1) (2020), https://doi.org/10.1136/bmjdrc-2019-000982.
- [60] M. Kelleher, A. Dunn-Galvin, J.O. Hourihane, D. Murray, L.E. Campbell, W.H. I. McLean, A.D. Irvine, Skin barrier dysfunction measured by transepidermal water loss at 2 days and 2 months predates and predicts atopic dermatitis at 1 year, J. Allergy Clin. Immunol. 135 (4) (2015) 930–935 e1, https://doi.org/10.1016/j.jaci.2014.12.013.
- [61] S. Jansen van Rensburg, A. Franken, J.L. Du Plessis, Measurement of transepidermal water loss, stratum corneum hydration and skin surface pH in occupational settings: a review, Skin Res. Technol. 25 (5) (2019) 595–605, https://doi.org/10.1111/srt.12711.
- [62] G. Landini, G. Martinelli, F. Piccinini, Colour deconvolution: stain unmixing in histological imaging, Bioinformatics 37 (10) (2021) 1485–1487, https://doi.org/ 10.1093/bioinformatics/btaa847.
- [63] E.G. Medrano, S.E. Haydel, Complete genome sequence of the methicillin-resistant Staphylococcus aureus strain SQL1/USA300, used for testing the antimicrobial properties of clay phyllosilicates and customized aluminosilicates, Microbiol Resour Announc 10 (45) (2021) e0086121, https://doi.org/10.1128/MRA.00861-21.
- [64] J. Chen, S. Liao, Z. Xiao, Q. Pan, X. Wang, K. Shen, S. Wang, L. Yang, F. Guo, H. F. Liu, Q. Pan, The development and improvement of immunodeficient mice and humanized immune system mouse models, Front. Immunol. 13 (2022) 1007579, https://doi.org/10.3389/fimmu.2022.1007579.
- [65] M.P. Olekson, R.A. Faulknor, H.C. Hsia, A.M. Schmidt, F. Berthiaume, Soluble receptor for advanced glycation end products improves stromal cell-derived factor-1 activity in model diabetic environments, Adv. Wound Care 5 (12) (2016) 527–538, https://doi.org/10.1089/wound.2015.0674.
- [66] J. Michaels, S.S. Churgin, K.M. Blechman, M.R. Greives, S. Aarabi, R.D. Galiano, G. C. Gurtner, db/db mice exhibit severe wound-healing impairments compared with other murine diabetic strains in a silicone-splinted excisional wound model, Wound Repair Regen. 15 (5) (2007) 665–670, https://doi.org/10.1111/j.1524-475X.2007.00273.x.
- [67] Q. Lu, X. Hu, X. Wang, J.A. Kluge, S. Lu, P. Cebe, D.L. Kaplan, Water-insoluble silk films with silk I structure, Acta Biomater. 6 (4) (2010) 1380–1387, https://doi.org/ 10.1016/j.actbio.2009.10.041.
- [68] X.H. Zong, P. Zhou, Z.Z. Shao, S.M. Chen, X. Chen, B.W. Hu, F. Deng, W.H. Yao, Effect of pH and copper(II) on the conformation transitions of silk fibroin based on

- EPR, NMR, and Raman spectroscopy, Biochemistry 43 (38) (2004) 11932–11941, https://doi.org/10.1021/bi049455h.
- [69] P. Zhou, X. Xie, D.P. Knight, X.H. Zong, F. Deng, W.H. Yao, Effects of pH and calcium ions on the conformational transitions in silk fibroin using 2D Raman correlation spectroscopy and 13C solid-state NMR, Biochemistry 43 (35) (2004) 11302–11311, https://doi.org/10.1021/bi049344i.
- [70] B. Holt, A. Tripathi, J. Morgan, Viscoelastic response of human skin to low magnitude physiologically relevant shear, J. Biomech. 41 (12) (2008) 2689–2695, https://doi.org/10.1016/j.jbiomech.2008.06.008.
- [71] H. Li, P.Z. Toh, J.Y. Tan, M.T. Zin, C.Y. Lee, B. Li, M. Leolukman, H. Bao, L. Kang, Selected biomarkers revealed potential skin toxicity caused by certain copper compounds, Sci. Rep. 6 (2016) 37664, https://doi.org/10.1038/srep37664.
- [72] I.C. Lee, J.W. Ko, S.H. Park, J.O. Lim, I.S. Shin, C. Moon, S.H. Kim, J.D. Heo, J. C. Kim, Comparative toxicity and biodistribution of copper nanoparticles and cupric ions in rats, Int J Nanomedicine 11 (2016) 2883–2900, https://doi.org/10.2147/LIN.S106346
- [73] H. Tang, M. Xu, X. Zhou, Y. Zhang, L. Zhao, G. Ye, F. Shi, C. Lv, Y. Li, Acute toxicity and biodistribution of different sized copper nano-particles in rats after oral administration, Mater Sci Eng C Mater Biol Appl 93 (2018) 649–663, https://doi. org/10.1016/j.msec.2018.08.032.
- [74] I. Cichon, W. Ortmann, A. Bednarz, M. Lenartowicz, E. Kolaczkowska, Reduced neutrophil extracellular trap (NET) formation during systemic inflammation in mice with menkes disease and wilson disease: copper requirement for NET release, Front. Immunol. 10 (2019) 3021, https://doi.org/10.3389/fimmu.2019.03021.
- [75] D. Ghosh, C.M. Salinas, S. Pallod, J. Roberts, I.R.S. Makin, J.R. Yaron, R.S. Witte, K. Rege, Temporal evaluation of efficacy and quality of tissue repair upon laseractivated sealing, Bioengineering & Translational Medicine (2022) e10412, https://doi.org/10.1002/btm2.10412 n/a(n/a).
- [76] P. Krzyszczyk, R. Schloss, A. Palmer, F. Berthiaume, The role of macrophages in acute and chronic wound healing and interventions to promote pro-wound healing phenotypes, Front. Physiol. 9 (2018) 419, https://doi.org/10.3389/ fphys.2018.00419.
- [77] R.A. Crompton, H. Williams, L. Campbell, L. Hui Kheng, C. Saville, D.M. Ansell, A. Reid, J. Wong, L.A. Vardy, M.J. Hardman, S.M. Cruickshank, An epidermalspecific role for Arginase1 during cutaneous wound repair, J. Invest. Dermatol. 142 (4) (2022) 1206–1216 e8, https://doi.org/10.1016/j.jid.2021.09.009.
- [78] E. Bosch-Rué, L. Díez-Tercero, R. Rodríguez-González, B.M. Bosch-Canals, R. A. Perez, Assessing the potential role of copper and cobalt in stimulating angiogenesis for tissue regeneration, PLoS One 16 (10) (2021) e0259125, https://doi.org/10.1371/journal.pone.0259125.
- [79] J. Salvo, C. Sandoval, Role of copper nanoparticles in wound healing for chronic wounds: literature review, Burns Trauma 10 (2022) tkab047, https://doi.org/ 10.1093/burnst/tkab047.

- [80] K.M. McAndrews, T. Miyake, E.A. Ehsanipour, P.J. Kelly, L.M. Becker, D. J. McGrail, H. Sugimoto, V.S. LeBleu, Y. Ge, R. Kalluri, Dermal alphaSMA(+) myofibroblasts orchestrate skin wound repair via beta1 integrin and independent of type I collagen production, EMBO J. 41 (7) (2022) e109470, https://doi.org/10.15252/embj.2021109470.
- [81] F. Cialdai, C. Risaliti, M. Monici, Role of fibroblasts in wound healing and tissue remodeling on Earth and in space, Front. Bioeng. Biotechnol. 10 (2022) 958381, https://doi.org/10.3389/fbioe.2022.958381.
- [82] A.M. Sousa, T. Liu, O. Guevara, J. Stevens, B.L. Fanburg, M. Gaestel, D. Toksoz, U. S. Kayyali, Smooth muscle alpha-actin expression and myofibroblast differentiation by TGFbeta are dependent upon MK2, J. Cell. Biochem. 100 (6) (2007) 1581–1592, https://doi.org/10.1002/jcb.21154.
- [83] B. Hinz, S.H. Phan, V.J. Thannickal, M. Prunotto, A. Desmouliere, J. Varga, O. De Wever, M. Mareel, G. Gabbiani, Recent developments in myofibroblast biology: paradigms for connective tissue remodeling, Am. J. Pathol. 180 (4) (2012) 1340–1355, https://doi.org/10.1016/j.ajpath.2012.02.004.
- [84] Y. Tai, E.L. Woods, J. Dally, D. Kong, R. Steadman, R. Moseley, A.C. Midgley, Myofibroblasts: function, formation, and scope of molecular therapies for skin fibrosis, Biomolecules 11 (8) (2021), https://doi.org/10.3390/biom11081095.
- [85] L. Van De Water, S. Varney, J.J. Tomasek, Mechanoregulation of the myofibroblast in wound contraction, scarring, and fibrosis: opportunities for new therapeutic intervention, Adv. Wound Care 2 (4) (2013) 122–141, https://doi.org/10.1089/ wound.2012.0393.
- [86] N. Wilson, A. McArdle, D. Guerin, H. Tasker, P. Wareing, C.S. Foster, M.J. Jackson, L.E. Rhodes, Hyperthermia to normal human skin in vivo upregulates heat shock proteins 27, 60, 72i and 90, J. Cutan. Pathol. 27 (4) (2000) 176–182, https://doi. org/10.1034/j.1600-0560.2000.027004176.x.
- [87] I.J. Benjamin, D.R. McMillan, Stress (heat shock) proteins: molecular chaperones in cardiovascular biology and disease, Circ. Res. 83 (2) (1998) 117–132, https://doi. org/10.1161/01.res.83.2.117.
- [88] G. Wilmink, S. Opalenik, J. Beckham, M. Mackanos, L. Nanney, C. Contag, J. Davidson, E.D. Jansen, *In-vivo* optical imaging of hsp70 expression to assess collateral tissue damage associated with infrared laser ablation of skin, J. Biomed. Opt. 13 (5) (2008) 054066.
- [89] P. Tonino, C. Abreu, Microvessel density is associated with VEGF and alpha-SMA expression in different regions of human gastrointestinal carcinomas, Cancers 3 (3) (2011) 3405–3418, https://doi.org/10.3390/cancers3033405.
- [90] E.L. Nussbaum, T. Mazzulli, K.P. Pritzker, F.L. Heras, F. Jing, L. Lilge, Effects of low intensity laser irradiation during healing of skin lesions in the rat, Lasers Surg Med 41 (5) (2009) 372–381, https://doi.org/10.1002/lsm.20769.